High-Resolution Spatial Transcriptomic Atlas of Mouse Soleus Muscle: Unveiling Single Cell and Subcellular Heterogeneity in Health and Denervation

Jer-En Hsu[1], Lloyd Ruiz[1], Yongha Hwang[1,2], Steve Guzman[1], Chun-Seok Cho[1], Weiqiu Cheng[3], Yichen Si[3], Peter Macpherson[1], Mitchell Schrank[1], Goo Jun[4], Hyun-Min Kang[3]*, Myungjin Kim[1]*, Susan Brooks[1]* & Jun Hee Lee[1]*

[1]Department of Molecular & Integrative Physiology, University of Michigan, Ann Arbor, MI, USA
[2]Space Planning and Analysis, University of Michigan, Ann Arbor, MI, USA
[3]Department of Biostatistics, University of Michigan, Ann Arbor, MI, USA
[4]Human Genetics Center, University of Texas Health Science Center at Houston, Houston, TX, USA.

*Correspondence: hmkang@umich.edu, myungjin@umich.edu, svbrooks@umich.edu, leeju@umich.edu

Abstract

Skeletal muscle is essential for both movement and metabolic processes, characterized by a complex and ordered structure. Despite its importance, a detailed spatial map of gene expression within muscle tissue has been challenging to achieve due to the limitations of existing technologies, which struggle to provide high-resolution views. In this study, we leverage the Seq-Scope technique, an innovative method that allows for the observation of the entire transcriptome at an unprecedented submicron spatial resolution. By applying this technique to the mouse soleus muscle, we analyze and compare the gene expression profiles in both healthy conditions and following denervation, a process that mimics aspects of muscle aging. Our approach reveals detailed characteristics of muscle fibers, other cell types present within the muscle, and specific subcellular structures such as the postsynaptic nuclei at neuromuscular junctions, hybrid muscle fibers, and areas of localized expression of genes responsive to muscle injury, along with their histological context. The findings of this research significantly enhance our understanding of the diversity within the muscle cell transcriptome and its variation in response to denervation, a key factor in the decline of muscle function with age. This breakthrough in spatial transcriptomics not only deepens our knowledge of muscle biology but also sets the stage for the development of new therapeutic strategies aimed at mitigating the effects of aging on muscle health, thereby offering a more comprehensive insight into the mechanisms of muscle maintenance and degeneration in the context of aging and disease.

Introduction

Skeletal muscle plays a vital role in myriad physiological processes, including movement, posture maintenance, and metabolic regulation [1]. This complex tissue, characterized by its ability to convert chemical energy into mechanical force, is essential not only for physical activity but also for overall health and well-being. The architecture of skeletal muscle is remarkably intricate, featuring a variety of myofiber types, each with distinct functional and metabolic properties, and is interspersed with non-myocyte cells such as immune cells, fibroblasts, and endothelial cells. These diverse elements contribute to the muscle's cellular heterogeneity, with each type playing a specific role in muscle physiology and response to stimuli [2-4].

Skeletal muscle exhibits a profound dependency on neural inputs; innervation is crucial for maintaining muscle tone and function [5]. Denervation, the loss of neural input, leads to rapid atrophy and functional impairment, a process that is not only relevant to traumatic injuries and in various neuromuscular diseases but also plays a significant role in the aging process [6]. This dynamic interplay between muscle and nerve highlights the importance of understanding muscle biology in a holistic manner. The molecular makeup of skeletal muscles, which includes a diverse array of proteins, enzymes, and signaling molecules, further underpins their dynamic adaptability to various physical demands and stressors, as well as their response to changes in innervation status. Thus, a comprehensive understanding of the detailed structure and function of skeletal muscle, encompassing its heterogeneity and complex interactions with neural inputs, is pivotal. Such knowledge is essential not only for advancing our understanding of muscle physiology but also for developing targeted therapies for muscle-related diseases and addressing the challenges of muscle deterioration with aging.

Single-cell transcriptomic technologies have brought significant insights into cellular heterogeneity across various biological systems, yet their application in skeletal muscle research is challenged by the unique nature of muscle tissue. The elongated and multinucleate structure of myofibers is not amenable to standard fluidics or microwell-based cell sorting techniques, which are designed for smaller, mononucleate cells. In response to these challenges, single-nucleus RNA sequencing (snRNA-seq) has emerged as an alternative, focusing on the analysis of individual nuclei instead of whole cells [4]. Indeed, in several recent studies, snRNA-seq successfully profiled muscle tissues and revealed transcriptome heterogeneity in individual myonuclei [7-11]. However, it still showed several limitations in providing a complete picture of the transcriptomic activity of cells and tissues. First, it captures only the nuclear transcriptome, potentially missing critical information contained within the cytoplasm [12]. This exclusion is particularly significant in muscle fibers, where key elements of the cellular machinery and signaling pathways are often located in the cytoplasm. More importantly, snRNA-seq provides no information on the spatial organization of these nuclei within different regions of the muscle fibers, an aspect crucial to understanding the complex interactions and functionality of skeletal muscle.

The limitations of single-cell and single-nucleus approaches have led researchers to explore spatial transcriptomics, a technique that preserves the spatial context of gene expression within tissues. Spatial transcriptomics provides a two-dimensional map of transcriptomic data, allowing researchers to visualize gene expression patterns in relation to the tissue architecture [13-15]. Several recent studies used this technique to understand muscle transcriptome in health and disease states [16-18]. However, this method faced significant challenges when applied to skeletal muscle research. One major limitation is the resolution; current spatial transcriptomics techniques, such as the 10X Visium platform, offer a resolution that is often too coarse to distinguish individual cells or subcellular structures, such as the intricate arrangement of muscle fibers and neuromuscular junctions [16-18]. This limitation means that the heterogeneity and complex interactions within skeletal muscle tissue can be obscured, with the resulting data representing a mixture of signals from multiple cell types. Furthermore, these data were captured from muscle cross-sections, making it even more difficult to resolve cell types at specialized regions, such as the neuromuscular junctions. Consequently, while commercially available spatial transcriptomics platforms add valuable context to transcriptomic analysis, its current resolution constraints limit its ability to provide the detailed insights necessary for a complete understanding of the nuanced cellular and molecular dynamics of skeletal muscle.

To overcome the limitations of traditional single-cell and spatial transcriptomics in skeletal muscle research, we employed Seq-Scope, a cutting-edge method that dramatically enhances spatial resolution and analytical depth [13-15, 19, 20]. Seq-Scope, characterized by its ability to provide ultra-high spatial resolution transcriptomic data, allows for the precise mapping of gene expression at the subcellular level. This advanced technology enabled us to conduct a comprehensive profiling of both normal skeletal muscle and its response to denervation along the longitudinal axis of muscle fibers. Our findings, with unprecedented detail, reveal not only the intricate structure of neuromuscular junctions (NMJs) but also the heterogeneous responses of muscle fibers to denervation. Furthermore, our high-resolution data illuminate the complex interactions between myofibers and non-muscle cells, both of which undergo substantial changes in their transcriptome phenotypes during denervation responses. This study thus represents a significant advancement in the field of muscle biology, providing a foundation for future research into the molecular mechanisms of muscle function and disease.

Results

Seq-Scope Profiling of Mouse Soleus Muscle

After our initial publication of Seq-Scope, which utilized a MiSeq flow cell to monitor 1 mm diameter circles [20], we expanded its applicability to include a HiSeq flow cell [21], providing a wider imaging area of 1.5 mm x 60 mm in a rectangular shape. This advancement enables the examination of larger tissue samples, such as the whole mouse soleus muscle, which fits well within this area. Among different muscle tissues, the soleus muscle is attractive for transcriptome analysis due to its mixed composition of both type I and type II fibers, each endowed with distinct physiological properties. Type I fibers are rich in mitochondria and suited for endurance, while type II fibers display a wide range of metabolic properties and are adapted for rapid, powerful movements. In addition, the mouse soleus has a relatively simple architecture with individual muscle fibers running over 70% of the length of the muscle and arranged parallel to the long axis. Finally, the neuromuscular junctions are aligned in a narrow band across the muscle. These features make the soleus muscle an ideal model for a comprehensive exploration of the skeletal muscle transcriptome, providing insights into the varied functional capabilities of muscle fibers under different physiological conditions.

In our initial experiments, we examined 7 longitudinal sections of fresh frozen mouse soleus muscle (Fig. S1A), among which 5 were successfully profiled for the entirety of the soleus muscle tissue sectioned longitudinally (approximately 6-7 mm; Fig. S1B), with the exception of the terminal structures connected to tendons. 2 additional sections were also partially profiled. The entire dataset revealed 28.8 million unique reads aligned to transcriptome. The distribution of detected transcripts showed an interesting pattern where the concentration of discovered transcripts was relatively lower at the center of the myofibers, while the concentration was very high at the fiber periphery (Fig. S1C). This is consistent with microscopic arrangements where the center of a myofiber is occupied with densely-packed myofibrils, while nuclear and other cytoplasmic structures, which presumably contains most of transcripts, are located at the periphery.

Identification of Major Fiber Types through Myofiber segmentation

Image-based cell segmentation is one of the approaches to leverage the high-resolution feature of Seq-Scope [20]. We utilized the H&E histology images of the exact same section that produced the dataset to manually segment the spatial area and aggregate the dataset according to individual myofiber boundaries (Fig. 1A). Through segmentation of the five and a half sections, we obtained 1,355 myofiber transcriptomes. After applying a cutoff of a minimum of 300 gene features and filtering out all mitochondrially encoded transcripts, hemoglobins and hypothetical gene models, each myofiber contains a median and mean ± SD of 1,174 and 1,680 ± 1,281 gene features (Fig. 1B) and 2,732 and 5,903 ± 8,732 unique transcripts (Fig. 1C). The high variability in gene and transcript numbers reflects that, due to the longitudinal sectioning scheme, myofiber area is variably represented in the tissue section. Still, high-dimensional clustering analysis was effective in identifying three distinct group of fibers representing type I (MF1), type IIa (MF2A) and type IIx (MF2X) fibers (Fig. 1D). Major markers for these clusters (Fig. 1E-1G, S1D) included myosin heavy chain marking each of the fiber types (*Myh7* for MF1, *Myh2* for MF2A and *Myh1* for MF2X; first row of Fig. 1H). Other markers that show differential expression across fiber type (MF1-MF2A-MF2X) axis include tropomyosins (*Tpm3* for MF1, and *Tpm1* for MF2X; second row of Fig. 1H), troponins (e.g. *Tnnt1* for MF1, and *Tnnt3* for MF2X; second row of Fig. 1H), ER calcium pumps (*Atp2a2* for MF1, and *Atp2a1* for MF2X fiber; third row of Fig. 1H) and metabolic enzymes (*Idh2*, key enzyme for Krebs cycle, and *Aldoa*, key enzyme for glycolysis; third row of Fig. 1H). The fiber type-specific gene marker list isolated from this analysis is largely congruent with former fiber type markers isolated from snRNA-seq datasets of mouse soleus muscle [7, 8]. Still, Seq-Scope analysis isolated many markers that were missed in former datasets (Fig. 1I), including *Cryab* that was previously shown to be expressed highly in type I fibers [22]. The spatial distribution of these myofiber transcriptome phenotypes was aligned in the histological space according to their segmented polygonal boundaries (Fig. 1J).

Analyses including mitochondrial and hypothetical genes, which led to median and mean ± SD expression of 4,802 and 10,747 ± 16,530 transcripts and 1,178 and 1,610 ± 1,281 genes in 1,365 cells after a 300 gene feature cutoff, revealed the similar clustering results representing the three myofiber types (MF1, MF2A and MF2X; Fig. S1E). Interestingly, compared to the oxidative fibers, glycolytic fibers such as MF2X fibers expressed higher levels of various mitochondrial enzymes (Fig. S1F, S1G), indicating that, even though their oxidative metabolism is relatively suppressed, their mitochondria still produce transcripts encoding these genes that are essential for oxidative phosphorylation.

Identification of Hybrid Myofiber Phenotypes through Grid-based Cell Type Mapping

While cell segmentation is useful for analyzing high-resolution spatial datasets, its effectiveness is limited due to difficulties in segmenting certain cell types and, importantly for skeletal muscle, capturing intracellular transcriptome heterogeneity of multinucleate myofibers. To comprehend the entirety of the spatial transcriptome without segmentation bias, we performed uniform gridding using 14 µm-sided hexagonal array (Fig. S2A). After filtering out mitochondrial and hypothetical gene models (hemoglobins are maintained in the dataset to locate the blood vessels), and after applying a cutoff of 100 gene features, we obtained 28,570 hexagonal areas, and each of the areas revealed a median and mean ± SD expression of 310 and 381 ± 252 transcripts (Fig. S2B, S2C). The 100 gene feature cutoff was sufficient to remove the background and isolate the area covered by the muscle tissues (Fig. 2A and 2B). Even though the number of observed transcripts was small, multi-dimensional clustering analysis of this dataset was able to reveal most known major cell types in the tissue, including some novel subcellular features (Fig. 2C-2F, 3-4 and S3-S4).

The largest transcriptome clusters from multi-dimensional clustering analysis represent different myofiber types. The hexagonal clustering revealed detailed fiber types (Fig. 2E), similar to those observed in segmentation-based clustering (Fig. 1). This hexagonal data also pinpointed the precise spatial locations of each transcriptome phenotype (Fig. 2C, 2D, and 2F), forming a geometry roughly similar to what was revealed by segmentation-based analysis (Fig. 1J). However, the hexagon-based approach uncovered several critical details missing from the segmentation-based analysis.

Firstly, in cell type clustering, the hexagonal data identified Type IIb fibers (MF2B) —very fast, glycolytic fibers marked by the characteristic myosin heavy chain gene *Myh4*, which are rare in the mouse soleus, a muscle enriched with oxidative fibers. Intrigued by this discrepancy, we closely examined the spatial myofiber type mapping results. High-resolution cell type mapping analysis using multiscale sliding windows [20, 23] revealed that, while the spatial mapping of hexagonal myofiber types resembles that of segmented myofiber types, hexagonal data uncovered intra-myofiber heterogeneity. This heterogeneity shows different myofiber type transcriptomes within the same myofiber area. The presence of different myosin heavy chain isoforms in a single myofiber, termed 'hybrid myofiber', was previously identified through a single molecule FISH approach, and found to be common in the soleus muscle [7, 8]. Consistent with these studies, we observed mixtures of MF2A and MF2X, or MF2X and MF2B (Fig. 2G). Additionally, we found that, as expected given the rarity of MF2B in mouse soleus, the MF2B phenotype did not occupy the whole myofiber, and only appeared in a hybrid fiber combined with the MF2X phenotype (Fig. 2F, 2G). Such characteristics would have rendered the MF2B phenotype undetectable in the segmentation-based analysis (Fig. 1).

Despite these minor discrepancies, the fiber-type-specific markers isolated from hexagonal analysis (Fig. 2H), including well-characterized myosin heavy chain genes (Fig. 2I), generally align well with those identified from segmentation-based analysis (Fig. S2D) and previous snRNA-seq analyses (Fig. 2J).

We also detected some myofiber clusters exhibiting higher levels of cathepsin B (MFDEGEN in Fig. 2K and 2L), which were formerly associated with an exercise effect [24] or muscle degeneration [25]. However, these areas were scattered over the histological area without specific patterns (Fig. 2L).

Characterization of Non-Myocytes in Seq-Scope Dataset

Hexagonal analysis also revealed a variety of non-myocyte transcriptome including macrophages (*Cd74* and MHC components), adipose tissue (*AdipoQ*, *Scd1* and *Cfd*), fibroblast (*Gsn*, *Dcn* and Collagens), smooth muscle (smooth muscle-specific actomyosin components) and erythrocyte (hemoglobins) transcriptome signatures (Fig. 3A-3D). Locations of these cell types corresponded well with histological findings; for example, smooth muscle transcriptomes were found around the areas where arteries are located (Fig. 3E, left panel). The Seq-Scope dataset identified well-characterized smooth muscle markers such as *Acta2*, *Myl9*, *Tagln* and *Mylk* (Fig. 3D). Interestingly, previous snRNA-seq datasets did not isolate these as the top markers for smooth muscle (Fig. S3A) [7, 8], suggesting that Seq-Scope can sensitively detect important biological signatures that can be overlooked by other analyses. As expected, nuclear-less erythrocyte transcripts were only discoverable from Seq-Scope dataset. Macrophage populations were also only detectable from Seq-Scope datasets, while being largely absent from snRNA-seq datasets. In contrast, snRNA-seq datasets contained some transcriptome components that are not well represented in Seq-Scope dataset, such as tenocytes, myotendius junctional nuclei and satellite cell transcriptome, which could be due to the nature of sections which might lead to volumetric underrepresentation of these cell types. In contrast, fibroblast markers from Seq-Scope dataset are similar to those of FAPS (Fibro/Adipogenic Progenitors) isolated from snRNA-seq studies (Fig. S3B), indicating some degree of conserved observation between the platforms, along with conserved myofiber type observations (Fig. 1I, 2J). Likewise, differentiated adipose tissue transcriptome with conventional adipocyte markers (Fig. 3D) was detected in areas where lipid-laden cells are found (Fig. 3E, right panel).

Characterization of Neuromuscular Junction (NMJ) Transcriptome in Seq-Scope Dataset

Other interesting features we identified through multi-dimensional clustering (Fig. 3B) were clusters corresponding to subcellular transcriptome structures, such as nuclei represented by the nucleus-specific non-coding RNAs *Malat1* and *Neat1* (Fig. 3D in ; highlighted in blue in Fig. 4A) [26]. We also discovered transcripts localized to an area corresponding to neuromuscular junctions (NMJ) (Fig. 3B in yellow; Fig. 4A in red). NMJ transcriptome, closely located to nuclear (NUC) cluster in the UMAP manifold (Fig. 4A in blue), contains many genes specifically expressed in postsynaptic nuclei, such as *Prkar1a*, *Etv5*, *Ufsp1* and *Chrna1* (Fig. 4B). The spatial areas for the NMJ transcriptome correspond very well with known histological locations of NMJ, which is located along the midline of soleus muscles (Fig.

4C). A magnified view of NMJ transcriptome areas showed that many of these areas overlapped with histological endplate structure, which represents a cluster of postsynaptic myonuclei (Fig. 4D, red ellipses). Indeed, many NMJ markers isolated from the Seq-Scope dataset overlapped well with postsynaptic nuclei markers in the previous snRNA-seq datasets (Fig. 4E), and explains why NMJ transcriptomes are similar to the NUC transcriptome as both represent nuclear transcriptomes. We also isolated NMJ areas that did not overlap well with endplate structures, and some NMJ markers, such as *Mpz* and *Smoc2*, are actually associated with either the myelinating or non-myelinating Schwann cell transcriptomes [27]. To isolate these cell types, we have subclustered the NMJ population (Fig. 4F); however, such subclustering only isolated fiber type-specific markers (Fig. 4G), which we isolated in the earlier analysis (Fig. 1, 2). Because the NMJ postsynaptic nuclei originate from myofibers, it is plausible that they preserve their corresponding fiber type identity. Therefore, we took an alternative approach where we spatially plotted all discovered NMJ marker genes and examined if we could identify a spatial area distinct from postsynaptic nuclei corresponding to the Schwann cell transcriptome. Interestingly, among the NMJ markers we isolated, *Mpz* and *Smoc2*, genes highly expressed in myelinating and non-myelinating Schwann cells [27], respectively, were spatially separated from the markers of postsynaptic myofiber nuclei [7-9], such as *Prkar1a*, *Etv5* and *Ufsp1* (Fig. 4H and 4I). In contrast, acetylcholine receptors were almost exclusively found at the postsynaptic nuclei area marked by *Prkar1a* expression (Fig. S4A). Based on the expression of *Mpz* and *Smoc2*, we have manually segmented additional spatial areas that likely represent myelinating and non-myelinating Schwann cells respectively (Fig. 4H and 4J). We performed another round of differential expression analysis based on their segmented transcriptomes compared to the postsynaptic area, defined by the expression of *Prkar1a* (Fig. 4K-4N). This analysis revealed many additional genes specifying the perisynaptic area (Fig. 4M) and the myelinating Schwann cell area (Fig. 4N). The perisynaptic transcriptome exhibited high expression of *Lum*, *Apod* and *Dcn*, in addition to *Smoc2* (Fig. 4M), which are all prominently represented in the previous non-myelinating Schwann cell transcriptome dataset [27] (Fig. 4L; Wolbert-nmSC). In contrast, the myelinating Schwann cell transcriptome in our dataset (Hsu-mySC) had genes involved in myelination, such as *Pmp22* [28] and *Ndrg1* [29], in addition to *Mpz* (Fig. 4N), again overlapping with the myelinating Schwann cell transcriptome (Fig. 4L; Wolbert-mySC) [27]. Interestingly, the perisynaptic transcriptome in our dataset (Hsu-perisynaptic) did not overlap with a recently generated perisynaptic terminal Schwann cell transcriptome dataset [30]. Nevertheless, *ApoD*, one of the most prominent perisynaptic area markers in our dataset (Fig. 5M) but missing from the terminal Schwann cell dataset [30], was confirmed to be highly expressed in the terminal Schwann cells in the RNAscope analysis [31]. *ApoD* was also detected in myelinating Schwann cells of intramuscular nerves [31], and this observation was also reproduced in our dataset (Fig. 5N). Plotting of these genes revealed the spatial arrangement of postsynaptic nuclei (reddish color in Fig. 4K and S4B), perisynaptic area (greenish color) and myelinating Schwann cell area (bluish color), which is congruent to known geometrical arrangements of Schwann cells and postsynaptic myofiber nuclei at the neuromuscular junction (Fig. 4J).

Fiber type-Specific Responses to Denervation

To enhance our understanding of how different muscle cells and compartments respond to denervation, we examined mouse soleus muscles at 3 and 7 days after denervation. In this experiment, the left soleus muscle was denervated, while the right was left as an uninjured innervated control (Fig. 5A). After obtaining spatial transcriptomes of these muscle tissues through Seq-Scope (Fig. 5B, 5C), the dataset was segmented into individual myofibers and subjected to a cell type mapping analysis through multi-dimensional clustering (Fig. 5D). After applying a gene feature cutoff of 300, we obtained 3908 segmented myofiber transcriptomes from control and denervated fibers at 3 days (1337 and 620, respectively) and 7 days (1127 and 824, respectively). After removing all mitochondrial, hypothetical and hemoglobin-encoding transcripts, the median and mean numbers of transcripts in each myofiber was 1738 and 3274 ± 5332 respectively (Fig. 5B). Not surprisingly, denervated fibers at 3 and 7 days (3D and 7D, respectively) exhibited transcriptomes substantially different from control fibers, while fibers from control muscles at 3 and 7 days integrated very well into each other (Fig. S5A), indicating that the experimental batch effect is negligible when compared to the large biological effects of denervation. Some of the fibers in day 7 denervated fibers contained a fibrotic signature, likely due to effects from fibroblast transcriptome nearby the myofibers. As we focused on myofiber transcriptomes, the fibers displaying fibrotic signatures were excluded from the fiber type-specific analysis (FIBRO in Fig. 5D; NA in Fig. 5E). In all muscles, we were able to identify at least three different myofiber types, which according to the expression analysis of myosin heavy chain, troponin and tropomyosin isoforms (Fig. S5B) corresponds to Type I, IIa and IIx fibers (Fig. 5D).

Even though classical markers, such as myosin heavy chain, troponin and tropomyosin isoforms, were relatively highly expressed in their corresponding myofiber types within the same section, allowing us to identify their original fiber types, their level was strongly diminished in day 3 denervated myofibers compared to control myofibers (Fig. S5B). In contrast, differential expression analyses identified a number of genes that were strongly upregulated in day 3 denervated fibers, and also explicitly upregulated in specific myofiber types, such as oxidative type I or glycolytic type IIx fibers (Fig. 5E). Markers enriched for day 3 denervated myofiber type I (D3-MF1) include several heat shock proteins (e.g. *Hspb1*, *Hspa8*), crystallins (*Cryab*) and muscle stress response proteins (e.g. *Csrp3*, *Ankrd1*), which were previously shown to be upregulated upon denervation in proteomic studies [32]. We found that these genes, in addition to the markers of damaged myofibers (e.g. *Xirp1*, *Flnc*, *Enah* and *Otud1*; see references [7, 9, 33]), were strongly upregulated in D3-MF1 compared to the other myofiber types (Fig. S5C). In contrast, markers enriched for day 3 denervated myofiber type IIx (D3-MF2X) included other types of heat shock proteins (e.g. *Hspb8*) and metallothioneins (*Mt1*, *Mt2*) (Fig. S5D).

Compared to the day 3 denervated myofibers, markers enriched for day 7 denervated fibers were much less obvious. Some classical myofiber markers, such as *Myh7* and *Tnnt1*, were found to be upregulated in day 7 denervated myofiber type I (D7-MF1; Fig. S5E), while other genes such as *Krt18*, *Cdkn1a* and *Ctsd*, were more highly upregulated in day 7 denervated myofiber type IIx (D7-MF2X; Fig. S5F). Interestingly, day 7 denervated fibers show upregulation of various genes responding to cellular stresses including autophagy controllers (Fig. S5G), atrophy inducers (Fig. S5H), a chromatin modulator (*Hdac3*; Fig. S5I) and oxygen metabolism genes (*Mb* and *Car3*; Fig. S5I), as well as DNA damage responsive transcripts (*Cdkn1a*, *Gadd45a* and *Mdm2*; Fig. S5J), which show variable fiber type specificities in regulation.

Fiber type-Specific Responses Were Robustly Observed Across Multiple Samples

To further our systematic analysis, we integrated normal and denervated datasets, and also added additional datasets with more sections from denervated animals. In total, 32 sections from 11 animals (untreated (C0; 3 mice, 12 sections), control at 3 days (C3; 1 mouse, 2 sections), control at 7 days (C7; 1 mouse, 2 sections), 3 days after denervation (D3; 2 mice, 6 sections) and 7 days after denervation (D7; 4 mice, 9 sections) were analyzed through Seq-Scope, and subjected to hexagonal gridding (Fig. 6A-6C) as done for the normal muscle dataset (Fig. 2). After filtering out mitochondrial and hypothetical gene models and after applying a cutoff of 100 gene features (Fig. S6A; which isolated the tissue-covered area as in Fig. 6C), we obtained 121,191 hexagonal area, and each of the areas revealed a median and mean ± SD expression of 248 and 311 ± 200 transcripts (Fig. S6B). The isolated hexagons were then subjected to cell type mapping through multi-dimensional clustering (Fig. 6D-6G).

Cell type mapping identified both myocellular and non-myocellular cell types. Myocellular transcriptome types are largely similar to what we have observed from segmentation-based myofiber analysis (Fig. 5), as we were able to identify three major fiber types (Type I, IIa and IIx) from control (MF1-N, MF2A-N, MF2X-N), 3 days after denervation (MF1-D3, MF2A-D3, MF2X-D3), and 7 days after denervation (MF1-D7, MF2A-D7, MF2X-D7) samples. Importantly, distribution of these clusters were reproducibly observed across different sections and animals (Fig. 6F) even though there were substantial changes in their composition (Fig. S6C) likely due to the variations in tissue section representation. Importantly, all untreated mouse samples and control samples isolated from denervated animals were integrated well into each other (Fig. 6E, 6F, S6C) regardless of sections and animals. Likewise, all D3 and D7 samples were integrated well into their corresponding cluster groups (Fig. 6E, 6F, S6C). Examination of cluster-specific markers for these myofibers (Fig. 6H) successfully reproduced major observations made by segmentation-based analysis (Fig. 5), including the presence of fiber type-specific denervation responses. For instance, induction of *Ankrd1*, *Hspb1* and *Cryab* in D3-MF1 as in Fig. S5C; *Hspb8*, *Mt1* and *Mt2* in D3-MF2X as in Fig. S5D; *Sln*, *Myh7*, *Tnnt1* in D7-MF1 as in Fig. S5E; *Krt18*, *Cdkn1a* and *Pvalb* in D7-MF2X as in Fig. S5F, were all reproduced in the hexagonal cluster marker analysis (Fig. 6H).

Non-Myocyte Responses to Denervation

The hexagonal datasets also revealed non-myocyte transcriptome clusters such as macrophage, smooth muscle, fibroblast and adipocyte clusters (Fig. 6G). Among these, we focused on macrophages and fibroblasts, which are likely to be profoundly associated with myofiber physiology. In the current analysis, we were able to identify 3 subclusters each for fibroblast and macrophage populations, designated as MACRO1-3 (Fig. S6D-S6L) and FIBRO1-3 clusters (Fig. S6M-S6U). Even though there are substantial variations in the frequency of occurrence for both myocytes and non-myocytes (Fig. S6C), we were able to observe a trend of increasing macrophage populations after denervation treatment (Fig. S6G-S6I). Expression of macrophage-specific markers also tend to increase after denervation, with the highest expression at 7 days post-denervation (Fig. S6J-S6L). These trends in population and gene expression were observed in all three subclusters of macrophages (MACRO1-3; Fig. S6G-S6L).

Fibroblasts, in contrast, did not show a clear trend of population level changes (Fig. S6P-S6R). However, FIBRO1 cluster (Fig. 6I) showed an interesting regulation in gene expression. Even though its population share did not change much after denervation in both 3 and 7 days (Fig. 6J), denervation clearly altered gene expression profiles of the FIBRO1 population, with unique gene signatures specific to day-3 and day-7 denervated muscle FIBRO1 cells (Fig. 6K). Such differential expression was observed throughout the examined samples even though there were slight variations across the samples (Fig. 6L). Specifically, the acute denervation response at 3 days is associated with strong upregulation of collagen (*Col3a1*), chemokine (*Cxcl14*), and cathepsin (*Ctsl*), and at 7 days with upregulation of extracellular matrix-encoding genes (*Fn1*, *Mgp*, *Dcn*) (Fig. 6K, 6L). These results reveal the dynamic changes associated with fibroblast denervation responses.

NMJ Responses to Denervation

Denervation entails the complete elimination of neuronal input to skeletal muscle, so we examined the response of the NMJ to denervation. In each condition, NMJ clusters scattered in the UMAP manifold, and NMJs from each section exhibited a transcriptome that was similar to their respective parental myofiber transcriptome (Fig. 7A). Differential expression analysis of NMJ markers showed that, similarly to the myofiber transcriptome responses (Fig. 5, 6), the NMJ transcriptome also upregulates damage response genes, such as heat shock proteins and crystallines (Fig. S7A, S7B), in response to denervation. The level of NMJ markers such as *Prkar1a* remained constant, while the level of an acetylcholine receptor subunit, *Chrna1* was strongly elevated (Fig. S7C). The rate of the NMJ population in the dataset does not change substantially after denervation (Fig. 7B), and many postsynaptic NMJ markers, including *Prkar1a*, *Etv4* and *Ufsp1*, were strictly confined to the NMJ structure throughout the course of the denervation experiment (Fig. 7C and S7D). Although most acetylcholine receptors were also exclusively expressed in the NMJ area and depleted in other myofiber areas in the uninjured control muscle, expression of some acetylcholine receptor isoforms, such as *Chrna1*, *Chrnb1* and *Chrng*, were consistently elevated throughout the denervated muscle fibers (Fig. 7D, 7E); in fact, the expression of *Chrnb1* and *Chrng* in the general myofiber area was even greater than its baseline expression in NMJ. All of these observations are consistent with the known regulation of acetylcholine receptor gene expression [34], which is suppressed by neuronal innervation. However, *Chrne* expression was still confined to NMJ area even after denervation (Fig. 7D), consistent with the previous finding that *Chrne* expression in postsynaptic nuclei is developmentally controlled at individual endplates [35]. Denervation-induced extrajunctional acetylcholine receptor subunit expressions were visually demonstratable in the spatial gene expression analysis (Fig. 7E). In this analysis, *Prkar1a*, *Etv4* and *Ufsp1* (red colors) are always confined to the postsynaptic NMJ area, while *Chrna1* and *Chrng* were massively upregulated (yellow colors Fig. 7E) throughout the histology section in denervated muscle tissues.

We also examined the gene expression profiles of other cell types in NMJ area, which can be identifiable from our Seq-Scope dataset (Fig. 4). Myelinating Schwann cell area, marked by *Mpz* and *Pmp22* expression, were not obviously detectable in denervated muscle tissues in contrast to normal muscle tissues where they were readily detectable (Fig. 4). Nevertheless, we were able to locate perisynaptic areas where we can find non-myelinating/terminal Schwann Cell marker expression (Fig. 7E; green colors), found in the vicinity of postsynaptic NMJs (Fig. 7E; red colors). We found that these perisynpatic markers exhibit more widespread expression after denervation (Fig. 7E; green colors), compared to the control muscle tissue. As done for normal muscle (Fig. 4), we have segmented post- and peri-synaptic NMJ area using these markers and performed the differential expression analysis between normal and denervated tissues. The analysis revealed that many transcripts involved in extracellular matrix (ECM) remodeling and injury response were specifically upregulated in the perisynaptic area (Fig. 7F-7I). Upregulation of these genes after denervation was also obvious in spatial plotting around the NMJ area (Fig. 7J). This is consistent with previous findings reporting the response of terminal Schwann cells to neuronal injury with proliferation and active remodeling of the ECM [36-39]. Since many of these genes are also expressed in other cell types, such as fibroblasts and macrophages, it is possible that additional cell types recruited to the NMJ site during denervation might also contribute to the remodeling activities.

High-Resolution Projection of Transcriptome Phenotypes Using FICTURE

To further comprehend the spatial distribution of different transcriptome phenotypes, we performed FICTURE analysis [40], which can perform spatial analysis at raw pixel-level resolution, in our case submicrometer resolution. Using FICTURE, we projected transcriptome phenotypes we learned from hexagonal gridding (Fig. 6) into the raw histological space and were able to obtain a high-resolution map of these phenotypes (Fig. S3C). Magnified analysis showed that, unlike in control innervated muscle, where fibroblasts and macrophages are limited to the area around the blood vessel containing smooth muscle arteries (Fig. S3D, S3E), denervated muscle at day 3 (Fig. S3F, S3G) and day 7 (Fig. S3H, S3I) exhibited a substantially increased presence of macrophage and fibroblast populations in the interstitial area of skeletal muscle. This increase was not limited to the area around the blood vessels or NMJ but was rather widespread across the entire span of the tissue. These observations align with histological findings, where numerous extra-myofiber nuclei were identified in the interstitial spaces (Fig. S3C-S3I); FICTURE was able to annotate the cell types of these nuclei, which turned out to be the heterogeneous populations of macrophages and fibroblasts (Fig. S3C-S3I), initially identified from earlier analysis (Fig. 6).

Discussion

Skeletal muscle function and health underpin numerous physiological processes which are vital to the overall health and well-being of an organism. Understanding the intricate dynamics of these tissues, particularly their cellular heterogeneity and response to stimuli such as denervation, is critical in the context of muscle aging and neuromuscular diseases. Advances in transcriptomic technologies have the potential to elucidate these complex dynamics, bringing about new insights that could help manage muscle-atrophy related conditions. While each technology has its limitations, in this study, we employed Seq-Scope, an advanced technique that offers ultra-high spatial resolution transcriptomic data at the single cell and subcellular level. This enabled us to conduct a comprehensive analysis of both normal and denervated skeletal muscle.

Importantly, our study is the first to provide the detailed transcriptomic atlas of mouse soleus muscle with microscopic spatial resolution, and to characterize the dynamic changes that occur following denervation. Previously, transcriptome-level studies in skeletal muscle were only conducted in scRNA/snRNA-seq platforms or the 10X VISIUM platform, which erases spatial information or only provides very coarse (100 µm center-to-center resolution) spatial information. Due to the limitations in spatial resolution, all spatial transcriptomics studies in skeletal muscle performed to date only utilized horizontal cross-sections [16-18], and therefore could not profile continuous transcriptomic mapping along the muscle fiber’s length and thus fails to address zonal differences along the longitudinal axis. By providing submicrometer-level spatial information while still characterizing whole transcriptome without target selection, we provided an unprecedented level of detail of how transcriptome structure is organized histologically in longitudinal section of the skeletal muscle.

To comprehend the vast amount of information in the dataset, we used two separate approaches; one based on histology-based myofiber segmentation and a second using uniform hexagonal grid-based spatial segmentation. These two methods of segmentation produced complementary results. For instance, even though both methods were successful in identifying major myofiber types, histology-based myofiber segmentation provided more robust clustering and more detailed differential gene expression analysis results. In contrast, hexagonal grid-based segmentation characterized transcriptome phenotypes in a manner agnostic to myofiber boundaries, leading to the identification of hybrid myofibers exhibiting a variety of transcriptome phenotypes that are uniquely localized to different subcellular portions of the myofibers. This dataset also profiles non-myocytes such as smooth muscle, macrophages, fibroblasts and adipocytes, as well as subcellular features such as myonuclei and NMJ, which all are congruent with their identified histological locations but were missed from the myofiber segmentation-based analyses. This transcriptome-level information was able to provide a detailed holistic overview of molecular makeup of skeletal muscle tissue across the longitudinal histology.

Our findings also underscore the complexity of skeletal muscle's response to denervation, highlighting the concomitant changes in both myofibers and non-myocytes. We identified fiber type-specific denervation responses, most pronounced at 3 days after denervation, which included disparate upregulation of heat shock proteins, crystallines, metallothioneins, autophagy-regulating genes, stress responsive genes, and genes regulating oxygen metabolism. Non-myocytes also responded to denervation; for instance, fibroblasts express collagens and chemokines at early stages and upregulate extracellular matrix proteins at later stages. NMJs also exhibited denervation responses. After denervation, some NMJ-specific genes such as those for some of the acetylcholine receptors subunits are no longer confined to the NMJ and become widespread across the myofibers, while others still show NMJ-specific expression. Postsynaptic nuclei share general myofiber responses to denervation, while perisynaptic cell types such as terminal Schwann cells and fibroblasts undergo expansion and upregulates many genes involved in extracellular matrix remodeling and wound healing responses.

Our data also reveal the involvement of damage-responsive pathways in denervation response, and uncover comprehensive patterns of gene regulation that was not formerly approachable. Our analysis shows that day 3 denervated myofiber type 1 (D3-MF1) strongly elevates the expression levels of several genes such as *Xirp1*, *Enah* and *Flnc*, which are involved in myofiber damage responses [33, 41, 42]. Notably, these genes were identified to be occasionally expressed in aged muscle myofibers or myofibers undergoing dystrophy [7, 9], indicating that such transcription is associated with denervation-induced changes. Consistent with this notion, we also found that day 7 denervated muscle tissue (D7) occasionally exhibited D3-MF1 myofiber transcriptome (Fig. S7E), which might provide a novel insight into muscle degeneration during denervation. Magnification of this area revealed that these myofibers are actually exhibiting hybrid property with both D3-MF1 and D7-MF1 transcriptome phenotypes. Interestingly, regions expressing D3-MF1 markers, such as damage markers *Xirp1*, *Enah* and *Flnc*, shows a degenerative pale H&E staining feature (Fig. S7F-S7H; yellow arrows), while regions expressing D7-MF1 markers showed normal myofiber pattern of H&E staining (Fig. S7F and S7H; blue arrows). These observations indicate that the damage-responsive transcriptome phenotypes are indeed associated with muscle degeneration after long term denervation. Most notably, these damage transcriptome (D3-MF1) markers show a partial co-localization with NMJ postsynaptic markers such as *Prkar1a*; D3-MF1 markers, however, showed more diffused patterns, while NMJ markers were more confined to the presumable NMJ region (Fig. S7G). This is an interesting observation suggesting that denervation-induced muscle injury signals may start from the NMJ area and propagate into distal myofiber areas before it completely degenerates.

In conclusion, our study represents a significant advancement in comprehending the detailed structure and function of skeletal muscle, particularly in response to denervation. By employing the state-of-the-art Seq-Scope technique, we were able to illuminate the complex interactions and heterogeneity within skeletal muscle, both at the level of individual myofibers, and in relation to the entire tissue. The insights derived have implications for developing targeted therapies for muscle-related diseases and addressing the age-associated muscle deterioration. However, it is important to emphasize that our findings are drawn from murine models, and further studies are necessary to validate our observations in human tissues and other clinical contexts. Nonetheless, our study underscores the power of advanced transcriptomic technologies for unravelling the cellular and molecular intricacies of skeletal muscle biology, and paves the way for future explorations in this important scientific domain.

Funding

The work was supported by the Taubman Institute Innovation Projects (to H.M.K. and J.H.L.), the NIH (T32AG000114 to C.S.C., K01AG061236 to M.K, R01AG079163 to M.K. and J.H.L., U01HL137182 to H.M.K., and UG3CA268091/UH3CA268091 to J.H.L., and P30AG024824, P30AG013283, P30DK034933, P30DK089503, P30CA046592, P30AR069620, and U2CDK110768), the Taiwanese Government Fellowship (to J.E.H), and the Glenn Foundation Core grants (to S.B. and J.H.L.).

Experimental Procedures

Mice Muscle Denervation Model

All animal procedures were subject to the regulations established by the University of Michigan Institutional Animal Care and Use Committee (IACUC). C57BL/6J mice littermates, approximately 6 months of age, underwent sciatic nerve transection (SNT) on their left hindlimb and were randomly assigned to a 3-day or 7-day recovery group. Mice were anesthetized using 5% isoflurane (MWI Animal Health) followed by continuous 2% isoflurane administration to ensure an unresponsive state to tactile stimuli. Preoperative analgesia was administered using 5 mg/kg carprofen (MWI Animal Health). The hindlimbs were shaved and cleaned with chlorhexidine and 70% alcohol. A small incision (<10 mm) was made 1 mm posterior and parallel to the femur to expose the sciatic nerve. The sciatic nerve was transected with a removal of a 5 mm segment, and the incision was closed with wound clips (Autoclip, BD Clay Adams). A sham procedure was replicated on the contralateral leg. Mice were placed on a heating pad after the procedure and monitored until full recovery from anesthesia. Mice recovered for either three or seven days before being sacrificed and tissue collection.

Seq-Scope array construction (1st-Seq)

Seq-Scope array was constructed as described previously [20]. Seq-Scope array is a solid phase transcriptome capturing system, which was constructed on the HiSeq2000 (Illumina) platform with HDMI32-DraI, a single-stranded oligonucleotide library (Eurofins), and Read1-DraI sequencing primer. Through sequence-by-synthesis strategy, 100pM HDMI32-DraI oligonucleotides were placed and formed into clusters on the flow cell surface. Sequencer was manually set to perform 37bp single-end reading with a custom Read1-DraI primer. The run was completed right after 37 cycles, and the flow cell was retrieved. The output FASTQ file from the run will provide the sequence and the XY coordinates of the barcodes. The retrieved flow cell was further processed into ready-to-use Seq-Scope array. The flow cell was washed with nuclease-free water three times and incubated with DraI (R0129, NEB) and CIAP (M0525, NEB) enzyme mixture in 37 ^{o}C overnight to expose oligo-dT end. The flow cell was then treated with exonuclease I (M2903, NEB) cocktail in 37 ^{o}C for 45 min to remove non-specific single-stranded DNA. In the last step, the flow cell underwent a series of washing steps, including three times with nuclease-free water, three times with 0.1N NaOH for 5 min each, and three times with 0.1M Tris pH7.5. The cover of the flow cell was then disassembled using Tungsten Carbide Tip Scriber (IMT-8806, IMT) to expose the surface of the array for tissue attachment.

Tissue Preparation, Sectioning, and processing

Mice subjected to SNT were anesthetized through intraperitoneal injection of 0.5 mg/g avertin (2,2,2,-Tribromoethanol 97%, Sigma #T48402, and 2-methyl-2-butanol 99%, Sigma #240486-100ml). Soleus muscles were freshly dissected and embedded into O.C.T compound (23-730-571, Fisher Scientific). The OCT blocks were snap-frozen by submerging into liquid nitrogen pre-chilled 2-Methylbutane (MX0760, Sigma-Aldrich). The sectioning of the OCT-mounted frozen tissue was performed in a cryostat (Leica

CM3050S, -15 °C) at a 5° cutting angle with each section 10 µm thick. Sections were attached to the array and re-warmed in room temperature. Attached sections were then fixed in 4% formaldehyde (15170, Electron Microscopy Sciences) in room temperature for 10 min, followed by hematoxylin and eosin (H&E) staining that was described previously [20]. H&E images were captured under the Keyence digital darkroom system.

Seq-Scope RNA Library Generation and Sequencing (2nd-Seq)

Seq-Scope library construction was constructed as described previously [20]. In brief, tissue sections were permeabilized with 0.2 U/µL collagenase I (17018-029, Thermo Fisher) at 37 °C for 20 min, followed with 1mg/mL pepsin (P7000, Sigma) in 0.1M HCl at 37 °C for 10 min. Permeabilized tissue sections were then washed with 1X Maxima RT buffer (EP0751, Thermofisher). Reverse transcription was conducted on the array through the incubation of RT mixture (1X RT buffer (EP0751, Thermofisher), 4% Ficoll PM-400 (F4375-10G, Sigma), 1mM dNTPs (N0477L, NEB), RNase inhibitor (30281, Lucigen), Maxima H-RTase (EP0751, Thermofisher)) in a humidified chamber at 42 °C overnight.

Tissue sections were treated with exonuclease I (#M2903, NEB) cocktail the next day in 37 °C for 45 min to remove unused single-stranded DNA probes. Sections were then incubated in tissue digestion cocktail (100 mM Tris pH 8.0, 100 mM NaCl, 2% SDS, 5 mM EDTA, 16 U/mL Proteinase K (P8107S, NEB)) at 37 °C for 40 min. After the tissues were digested, the array was washed three times with nuclease-free water, three times with 0.1N NaOH for 5 min each, and three times with 0.1M Tris pH7.5.

Secondary stand synthesis was conducted following the washing step. The array was loaded with secondary strand synthesis mixture (1X NEBuffer-2 (NEB), 10 uM TruSeq Read2-conjugated Random Primer (IDT), 1mM dNTPs (N0477, NEB), Klenow Fragment (M0212, NEB), and nuclease-free water) and incubated in a humidified chamber at 37 °C for 2 hr. Solution was removed upon the completion of the reaction, and the array was washed with nuclease-free water three times. The array was then treated with 0.1N NaOH for 5 min to elute the barcoded cDNA library. The pH of the elution was neutralized by 3 M potassium acetate, pH5.5. Eluted library was then further purified using AMPure XP beads (1.8X bead/sample ratio, A63881, Beckman Coulter) according to the manufacturer's instruction.

Library amplification was conducted through two rounds of PCR. First round PCR was performed using Kapa HiFi Hotstart Readymix (KK2602, KAPA Biosystems), 2µM forward and reverse primers as described in our previous paper [20], and the total eluted library. PCR product was purified using AMPure XP beads (A63881, Beckman Coulter) with 1.2X beads/sample ratio. Second round PCR was performed using Kapa HiFi Hotstart Readymix (KK2602, KAPA Biosystems), indexing primers described in [20], and 2nM of the first round PCR product. PCR product was purified again using AMPure XP beads (A63881, Beckman Coulter) with 0.6X beads/sample ratio. The size of the library was selected between 400-850bp through agarose gel electrophoresis. Selected library was purified using Zymoclean Gel DNA Recovery Kit (D4001, Zymo Research). The library was then sequenced with a paired-end (100-150bp) setup.

Generation of Spatial Digital Gene Expression (sDGE) Matrix

Data are processed as described previously [20, 23], combing both 1st-Seq and 2nd-Seq FASTQ results. In the processing, 2nd-Seq FASTQ results were first filtered for their presence in 1st-Seq data table, so that the alignment and data processing could be more efficient. Then alignment was performed in STAR to produce spatial digital gene expression matrix (sDGE) matching individual gene expression with spatial coordinates identified through HDMI matching between 1st-Seq and 2nd-Seq.

Alignment between histology and spatial dataset

From the dataset, spatial transcriptome density is visualized through hillshade function [43]. The hillshade image was semi-automatically aligned with H&E image using QGIS (version 3.22.9) georeferencer function, through manually marking salient spatial features common in both images.

Myofiber Segmentation and Hexagonal Gridding

Myofiber segmentation was performed on QGIS by manually drawing polygons on H&E images, according to myofiber boundary lines. Transcripts within each fiber were aggregated into a single datapoint, which was treated as a single cell located at a point on surface of the polygon. For hexagonal gridding, spatial data are aggregated toward a non-overlapping array of hexagons with 14µm sides, which was treated as a single cell located at the center of each hexagon.

Data Analysis and Visualization

The aggregated DGE matrix was analyzed in the Seurat package [44]. Feature number threshold was applied to remove the grids (as indicated in the figure and the text) that corresponded to the area that was not overlaid by the tissue. Data were normalized using SCTransform function. After discovering principal components through RunPCA and generating UMAP manifold using RunUMAP, clustering was performed using the shared nearest neighbor modularity optimization implemented in Seurat's FindNeighbors and FindClusters function, and then annotated to specific myofiber and cell types based on marker gene expression. For clustering segmented myofiber transcriptome from control/denervated dataset, clustering was sequentially performed, first to differentiate experimental conditions, and then to identify myofiber subtypes in each of experimental condition-dependent clusters. Clusters were visualized in histological space through plotting hexagonal centers using ggplot2 package (hexagonal dataset) or through plotting the whole polygonal area using geopandas and matplotlib package (segmentation dataset). FindMarkers and FindAllMarkers functions were used to identify Top markers from each cluster, and volcano plot was generated using the output of these functions using ggplot2. Level of gene expression was visualized though Seurat functions such as VlnPlot, DotPlot and FeaturePlot, and spatial gene expression was visualized through a custom visualization software which visualizes discovered genes as colored dots in the coordinate space. Gene expression analysis on aggregated datasets (e.g. myofiber segmented dataset and hexagonal dataset) was presented as SCT-normalized value, while spatial gene expression plot on raw coordinate histological plane was based on the raw gene expression data. For Area-proportional Venn diagrams were made using DeepVenn [16].

Overlapping hexagonal grid were generated to allow for multiscale sliding windows analysis [20, 23]. To make a projection, annotations provided from non-overlapping hexagonal analysis were fine tuned using FindTransferAnchors and TransferData in Seurat. Separately, factors learned from clusters of non-overlapping hexagonal analysis were projected into raw pixel-level dataset through FICTURE as described in our recent work [40].

References

1. Mukund, K. and S. Subramaniam, *Skeletal muscle: A review of molecular structure and function, in health and disease.* Wiley Interdiscip Rev Syst Biol Med, 2020. **12**(1): p. e1462.

2. Ritso, M., L.W. Tung, and F.M.V. Rossi, *Emerging skeletal muscle stromal cell diversity: Functional divergence in fibro/adipogenic progenitor and mural cell populations.* Exp Cell Res, 2022. **410**(1): p. 112947.

3. Schiaffino, S. and C. Reggiani, *Fiber types in mammalian skeletal muscles.* Physiol Rev, 2011. **91**(4): p. 1447-531.

4. Williams, K., K. Yokomori, and A. Mortazavi, *Heterogeneous Skeletal Muscle Cell and Nucleus Populations Identified by Single-Cell and Single-Nucleus Resolution Transcriptome Assays.* Front Genet, 2022. **13**: p. 835099.

5. Ehmsen, J.T. and A. Hoke, *Cellular and molecular features of neurogenic skeletal muscle atrophy.* Exp Neurol, 2020. **331**: p. 113379.

6. Soendenbroe, C., J.L. Andersen, and A.L. Mackey, *Muscle-nerve communication and the molecular assessment of human skeletal muscle denervation with aging.* Am J Physiol Cell Physiol, 2021. **321**(2): p. C317-C329.

7. Petrany, M.J., et al., *Single-nucleus RNA-seq identifies transcriptional heterogeneity in multinucleated skeletal myofibers.* Nat Commun, 2020. **11**(1): p. 6374.

8. Dos Santos, M., et al., *Single-nucleus RNA-seq and FISH identify coordinated transcriptional activity in mammalian myofibers.* Nat Commun, 2020. **11**(1): p. 5102.

9. Kim, M., et al., *Single-nucleus transcriptomics reveals functional compartmentalization in syncytial skeletal muscle cells.* Nat Commun, 2020. **11**(1): p. 6375.

10. Orchard, P., et al., *Human and rat skeletal muscle single-nuclei multi-omic integrative analyses nominate causal cell types, regulatory elements, and SNPs for complex traits.* Genome Res, 2021. **31**(12): p. 2258-2275.

11. Lin, H., et al., *Decoding the transcriptome of denervated muscle at single-nucleus resolution.* J Cachexia Sarcopenia Muscle, 2022. **13**(4): p. 2102-2117.

12. Denes, L.T., C.P. Kelley, and E.T. Wang, *Microtubule-based transport is essential to distribute RNA and nascent protein in skeletal muscle.* Nat Commun, 2021. **12**(1): p. 6079.

13. Tian, L., F. Chen, and E.Z. Macosko, *The expanding vistas of spatial transcriptomics.* Nat Biotechnol, 2023. **41**(6): p. 773-782.

14. Bressan, D., G. Battistoni, and G.J. Hannon, *The dawn of spatial omics.* Science, 2023. **381**(6657): p. eabq4964.

15. Kang, H.M. and J.H. Lee, *Spatial Single-Cell Technologies for Exploring Gastrointestinal Tissue Transcriptome.* Compr Physiol, 2023. **13**(3): p. 4709-4718.

16. D'Ercole, C., et al., *Spatially resolved transcriptomics reveals innervation-responsive functional clusters in skeletal muscle.* Cell Rep, 2022. **41**(12): p. 111861.

17. Heezen, L.G.M., et al., *Spatial transcriptomics reveal markers of histopathological changes in Duchenne muscular dystrophy mouse models.* Nat Commun, 2023. **14**(1): p. 4909.

18. Larouche, J.A., et al., *Spatiotemporal mapping of immune and stem cell dysregulation after volumetric muscle loss.* JCI Insight, 2023. **8**(7).

19. Gurkar, A.U., et al., *Spatial mapping of cellular senescence: emerging challenges and opportunities.* Nat Aging, 2023. **3**(7): p. 776-790.

20. Cho, C.-S., et al., *Microscopic examination of spatial transcriptome using Seq-Scope.* Cell, 2021. **184**(13): p. 3559-3572. e22.

21. Do, T.H., et al., *TREM2 macrophages induced by human lipids drive inflammation in acne lesions.* Sci Immunol, 2022. **7**(73): p. eabo2787.

22. Neufer, P.D. and I.J. Benjamin, *Differential expression of B-crystallin and Hsp27 in skeletal muscle during continuous contractile activity. Relationship to myogenic regulatory factors.* J Biol Chem, 1996. **271**(39): p. 24089-95.

23. Xi, J., et al., *STtools: a comprehensive software pipeline for ultra-high-resolution spatial transcriptomics data.* Bioinformatics Advances, 2022. **2**(1).

24. Gokce, E. and N. Gun, *The Relationship Between Exercise, Cathepsin B, and Cognitive Functions: Systematic Review.* Percept Mot Skills, 2023. **130**(4): p. 1366-1385.

25. Kar, N.C. and C.M. Pearson, *Early elevation of cathepsin B1 in human muscle disease.* Biochem Med, 1977. **18**(1): p. 126-9.

26. West, J.A., et al., *The long noncoding RNAs NEAT1 and MALAT1 bind active chromatin sites.* Mol Cell, 2014. **55**(5): p. 791-802.

27. Wolbert, J., et al., *Redefining the heterogeneity of peripheral nerve cells in health and autoimmunity.* Proc Natl Acad Sci U S A, 2020. **117**(17): p. 9466-9476.

28. Pantera, H., et al., *Regulation of the neuropathy-associated Pmp22 gene by a distal super-enhancer.* Hum Mol Genet, 2018. **27**(16): p. 2830-2839.

29. Berger, P., et al., *Expression analysis of the N-Myc downstream-regulated gene 1 indicates that myelinating Schwann cells are the primary disease target in hereditary motor and sensory neuropathy-Lom.* Neurobiol Dis, 2004. **17**(2): p. 290-9.

30. Castro, R., et al., *Specific labeling of synaptic schwann cells reveals unique cellular and molecular features.* Elife, 2020. **9**.

31. Seaberg, B.L., S. Purao, and M. Rimer, *Validation of terminal Schwann cell gene marker expression by fluorescent in situ hybridization using RNAscope.* Neurosci Lett, 2022. **771**: p. 136468.

32. Lang, F., et al., *Dynamic changes in the mouse skeletal muscle proteome during denervation-induced atrophy.* Dis Model Mech, 2017. **10**(7): p. 881-896.

33. Otten, C., et al., *Xirp proteins mark injured skeletal muscle in zebrafish.* PLoS One, 2012. **7**(2): p. e31041.

34. Tsay, H.J. and J. Schmidt, *Skeletal muscle denervation activates acetylcholine receptor genes.* J Cell Biol, 1989. **108**(4): p. 1523-6.

35. Yumoto, N., S. Wakatsuki, and A. Sehara-Fujisawa, *The acetylcholine receptor gamma-to-epsilon switch occurs in individual endplates.* Biochem Biophys Res Commun, 2005. **331**(4): p. 1522-7.

36. Proietti, D., et al., *Activation of skeletal muscle-resident glial cells upon nerve injury.* JCI Insight, 2021. **6**(7).

37. Love, F.M. and W.J. Thompson, *Schwann cells proliferate at rat neuromuscular junctions during development and regeneration.* J Neurosci, 1998. **18**(22): p. 9376-85.

38. Sugiura, Y. and W. Lin, *Neuron-glia interactions: the roles of Schwann cells in neuromuscular synapse formation and function.* Biosci Rep, 2011. **31**(5): p. 295-302.

39. Huang, X., J. Jiang, and J. Xu, *Denervation-Related Neuromuscular Junction Changes: From Degeneration to Regeneration.* Front Mol Neurosci, 2021. **14**: p. 810919.

40. Si, Y., et al., *FICTURE: Scalable segmentation-free analysis of submicron resolution spatial transcriptomics.* bioRxiv, 2023.

41. Molt, S., et al., *Aciculin interacts with filamin C and Xin and is essential for myofibril assembly, remodeling and maintenance.* J Cell Sci, 2014. **127**(Pt 16): p. 3578-92.

42. Leber, Y., et al., *Filamin C is a highly dynamic protein associated with fast repair of myofibrillar microdamage.* Hum Mol Genet, 2016. **25**(13): p. 2776-2788.

43. Horn, B.K.P., *Hill shading and the reflectance map.* Proceedings of the IEEE, 1981. **69**(1): p. 14-47.

44. Hao, Y., et al., *Dictionary learning for integrative, multimodal and scalable single-cell analysis.* Nat Biotechnol, 2023.

Figure Legends

Fig 1. Seq-Scope Analysis of Mouse Soleus Muscle Reveals Transcriptome Heterogeneity in Segmented Myofibers:

(A) Example of myofiber segmentation (right), based on H&E staining image (left). All transcriptome data in each segmented area are combined into a single data point (red circle, right) for individual myofiber analysis.

(B) Distribution of the number of gene features (nFeature_RNA), using a gene feature cutoff of 300 to select high-quality transcriptomes.

(C) Distribution of the number of unique transcripts (nCount_RNA) following the 300 gene feature cutoff.

(D) UMAP manifold of the myofiber transcriptome, showing three major fiber types identified via multidimensional clustering.

(E-G) Markers highly expressed in respective myofiber clusters were shown in volcano plot. The top 20 genes are highlighted in colors corresponding to those in (D).

(H) Expression of specific genes in indicated myofiber populations, presented as a violin plot. This includes myosin heavy chain (top), tropomyosins and troponins (middle), and ER calcium pumps and metabolic enzymes (bottom).

(I) Comparison between marker lists of each myofiber in this segmentation-based analysis (Hsu) and two previous single nucleus RNA sequencing studies [7, 8], using a Venn Diagram constructed with DeepVenn [16].

(J) Projection of segmented myofiber transcriptome clusters into histological space according to the segmented area. Upper panel visualizes the whole analysis area, while the lower two panels magnify the 4th and 5th sections in the upper panel.

Fig S1. High-Resolution Analysis of Skeletal Muscle Spatial Transcriptome Using Seq-Scope:

(A) Hematoxylin and eosin (H&E) staining of skeletal muscle (mouse soleus) longitudinal sections analyzed by Seq-Scope.

(B) Hillshade representation of RNA discovery density from the same section as in (A).

(C) Magnified comparison of H&E staining (center), RNA hillshade (right), and a merged image (left). Arrows highlight the transcripts concentrated at the boundary of myofibers.

(D) Dot plot showing marker genes enriched in each myofiber cluster, as presented in Fig. 1D.

(E) UMAP manifold of myofiber transcriptome, identified from the dataset including mitochondrial and hypothetical genes. The result is largely similar to the analysis excluding mitochondrial and hypothetical genes presented in Fig. 1D.

(F) Marker genes enriched in MF2X fibers, highlighting the high expression of many mitochondrial genes in these fibers.

(G) Expression patterns of myosin heavy chain genes and various mitochondrially encoded genes across different myofiber populations.

Fig 2. Histology-Agnostic Analysis of Skeletal Muscle Spatial Transcriptomics Reveals Subcellular Transcriptome Heterogeneity in Myofibers across Longitudinal Axis.

(A) Longitudinal section of mouse soleus muscle analyzed through H&E. These sections were used for all analyses in this figure.

(B-G) Seq-scope data were processed into uniform hexagonal grid with 14µm sides. Density of unique transcripts (B) and clustering results (C, D, F, G) were projected to histological space. UMAP representation of hexagonal transcriptome was shown with cluster-specific colors (E), which was also projected into histological space (D, G). Distribution of individual myofiber type was projected in red (F). Boxed areas are magnified according to their guiding lines.

(H) Cluster-specific marker genes were shown in volcano plot.

(I) Expression of myosin heavy chain isoforms, projected onto UMAP manifold.

(J) Comparison between marker lists of each myofiber transcriptome in this hexagonal analysis and two previous single nucleus RNA sequencing studies [7, 8], using a Venn Diagram constructed with DeepVenn [16].

(K and L) Markers isolated for MFDEGEN cluster (K) and its distribution in histological space (L).

Fig. S2. Hexagonal Analysis of Seq-Scope Dataset.

(A) Density of unique transcripts in hexagonal spatial dataset. Insets magnify the indicated area.

(B) Distribution of the number of gene features (nFeature_RNA) and unique transcripts (nCount_RNA), before using a gene feature cutoff of 100 to select high-quality transcriptomes.

(C) Distribution of the number of gene features (nFeature_RNA) and unique transcripts (nCount_RNA), after using a gene feature cutoff of 100 to select high-quality transcriptomes.

(D) Comparison between marker lists of each myofiber transcriptome in this hexagonal analysis (Hex) presented in Fig. 2 with the segmentation-based analysis (Fib) presented in Fig. 1.

Fig. 3. Non-Myocyte Transcriptomic Heterogeneity Revealed by Histology-Agnostic Analysis of Seq-Scope Dataset.

(A and B) Spatial plot (A) and UMAP manifold (B) presented in Fig. 2C and 2E were colored in a way that can highlight non-myocyte transcriptome.

(C) Spatial plot magnifying the boxed areas in (A) with corresponding colors.

(D) Dot plots visualizing the expression of cluster-specific top markers across different clusters.

(E) Boxed areas in (C) are further magnified according to the guiding line. Left panels highlight arteries while right panels highlight adipose tissue.

Fig. S3. Analysis of Seq-Scope Data for Non-Myocyte Transcriptome.

(A and B) Comparison for Smooth Muscle (A) and Fibroblast or Fibro–adipogenic progenitors (FAPs) marker (B) lists between the current hexagonal analysis and two previous single nucleus RNA sequencing studies [7, 8], using a Venn Diagram constructed with DeepVenn [16]. Top 20 significant genes were included in the analysis.

(C-I) FICTURE projection of cell types illustrated in Fig. 6 to the entire histological space with pixel-level resolution. The boxed areas in (C) are magnified in (D-I, top), and corresponding H&E images are shown (D-I, bottom). Highlighted regions include arteries (D, E, H, I), infiltrated macrophages and fibroblasts in interstitial area (F, G, H, I).

Fig. 4. Identification of Neuromuscular Junction-Associated Transcriptome from Seq-Scope Dataset.

(A) Identification of neuromuscular junction (NMJ, red) and nuclear (NUC, blue) transcriptome clusters from UMAP manifold of hexagonal Seq-Scope dataset. The manifold is same as Fig. 3B, but colored to highlight NMJ and NUC clusters.

(B) NMJ cluster-specific marker genes were highlighted in volcano plot. Top 10 markers are highlighted in red.

(C and D) Spatial plot of NMJ clusters in red (1th and 3rd in C), overlaid with histology (2nd and 4th in C). Boxed area in (C) is magnified in (D, left), and shown with the corresponding H&E only image (D, right).

(E) Comparison for NMJ marker lists between the current hexagonal analysis and two previous single nucleus RNA sequencing studies [7, 8], using a Venn Diagram constructed with DeepVenn [16]. Top 20 significant genes were included in the analysis.

(F and G) UMAP manifold illustrating isolated NMJ cluster (F), subclustered in three different colors (0 = red, 1 = green, 2 = blue), representing Type IIa, Type I and Type IIx myofibers, according to the marker analysis (G, as DotPlot). This suggests that NMJ postsynaptic nuclei maintain their originating fiber identities.

(H-J) Gene expression plot in indicated colors; gene detection is represented as dots. Red ovals represent postsynaptic area, green triangles represent perisynaptic area, and blue rectangles represent myelinating Schwann cell area (H, left). Boxed area in (H, right) is magnified in (I). Schematic illustration depicting NMJ structure (J).

(K-N) Isolation of additional markers representing different cell types in NMJ. Markers representing perisynaptic area (M) and myelinating Schwann cell area (N) are highlighted in volcano plots. Markers are compared with published marker lists for non-myelinating and myelinating Schwann cells [27] and terminal Schwann cells [30] (L). Top 20 significant genes were included in the DeepVenn [16] analysis. These genes were also plotted onto the magnified NMJ space (K), which shows geometry similar to typical NMJ structure (J).

Fig. S4. Expression of Different Marker Genes around the NMJ Area.

(A) Expression of different acetylcholine receptor isoforms around the postsynaptic nuclei marked by *Prkar1a* expression.

(B) Expression of different cell type markers, isolated in the analysis presented in Fig. 4, in different NMJ area.

Fig. 5. Heterogeneous Transcriptome Responses to Denervation in Different Myofibers.

(A) Schematic illustration of denervation experiment shown here. For each mouse, left hindlimb got denervation, while right hindlimb was saved as control. Tissues were collected after 3 and 7 days of treatment.

(B) Myofiber transcriptome isolated by H&E image-based segmentation was analyzed. Distribution of the number of gene features (nFeature_RNA), using a gene feature cutoff of 300 to select high-quality transcriptomes (left). Distribution of the number of unique transcripts (nCount_RNA) following the 300 gene feature cutoff (right).

(C) Hematoxylin and eosin (H&E, upper) staining of skeletal muscle (mouse soleus) longitudinal sections analyzed by Seq-Scope. Hillshade representation of RNA discovery density from the same sections (middle). Projection of segmented myofiber transcriptome clusters into space according to the area defined by H&E-based image segmentation. Cluster coloring corresponds to what is presented in (D)

(D) UMAP manifold of the myofiber transcriptome, showing the heterogeneous denervation responses in three major fiber types, identified via multidimensional clustering, in different colors.

(E) Identification of myofiber type-specific denervation response genes. Genes highly expressed in each myofiber type of day 3 denervated myofiber dataset are highlighted in volcano plot.

(F) Dot plots visualizing the expression of cluster-specific top markers across different clusters, highlighting fibertype-specific denervation responses.

Fig. S5. Fiber Type-Specific Denervation Responses.

(A) UMAP manifold of the myofiber transcriptome, colored by experimental conditions. All control samples clustered coherently, while day 3 and day 7 denervated samples showed clustering into corresponding groups.

(B-J) Expression of myosin heavy chain isoforms, tropomyosins and troponins (B), day 3 myofiber type I responses (C), day 3 myofiber type IIx responses (D), day 7 myofiber type I responses (E), day 7 myofiber type IIx responses (F), autophagy-related responses (G), atrophy responses (H), day 7-specific responses (I), and DNA damage responses (J), in major fibertype and denervation response clusters

Fig. 6. Systematic Analysis Identifies Heterogeneity in Both Myofiber and Non-Myocellular Denervation Responses.

(A-D) Spatial plot of experimental conditions (A), animal and section identity encoded by XXYZ, XX = experimental condition, Y = animal identity, Z = section identity (B), unique transcript density (C), transcriptome clustering results (D) colored as in (G). Spatial areas analyzed in Fig. 1-4 (red box) and Fig. 5 (cyan box) are indicated in (A).

(E-G) UMAP manifold colored by experimental conditions (A), animal and section identity (F) encoded as in (B), and clustering results (G).

(H) DotPlot of cluster-specific markers.

(I) UMAP manifold highlighting the FIBRO1 cluster, colored by experimental conditions. Other clusters were colored in background as light grey.

(J) Population shares of FIBRO1 cluster across different experimental conditions.

(K and L) Differential expression of FIBRO1 markers across different experimental conditions (K) and sections (L), visualized in DotPlot analysis.

Fig. S6. Denervation Responses in Non-Myocytes.

(A and B) Myofiber transcriptome isolated by hexagonal gridding was analyzed. Distribution of the number of gene features (nFeature_RNA), using a gene feature cutoff of 100 to select high-quality transcriptomes (A). Distribution of the number of unique transcripts (nCount_RNA) following the 100 gene feature cutoff (B).

(C) Distribution of different clusters across experimental conditions (left), animals identity (center), and section identity (right), encoded by XXYZ, XX = experimental condition, Y = animal identity, Z = section identity.

(D-O) UMAP manifold highlighting indicated clusters, colored by experimental conditions. Other clusters were colored in background as light grey.

(G-R) Population shares of indicated clusters across different experimental conditions.

(J-U) Differential expression of cluster-specific markers across different experimental conditions, visualized in DotPlot analysis.

Fig. 7. Denervation-Induced Changes around Neuromuscular Junction Area.

(A) UMAP manifold highlighting neuromuscular junction (NMJ) cluster, colored by experimental conditions. Other clusters were colored in background as light grey.

(B) Population shares of NMJ cluster across different experimental conditions.

(C and D) Differential expression of postsynaptic nuclei markers (C) and acetylcholine receptor isoforms (D) across different myofibers at different time points after denervation, visualized in DotPlot analysis.

(E) Expression of postsynaptic nuclei markers (warm colors) and non-myelinating perisynaptic Schwann cell markers (green colors) in control, 3 day denervated, and 7 day denervated myofibers, overlaid onto H&E images.

(F-I) Perisynaptic area-specific denervation responses at 7 days (F, H) and 3 days (G, I) were characterized through comparison over control perisynaptic area. The genes that were also regulated in postsynaptic area were removed from the analysis. The results are shown in volcano plot (F, G) and gene ontology (GO) enrichment analysis (H, I).

(J) Expression of postsynaptic nuclei markers (red colors), perisynaptic area markers (green colors), myelinating Schwann cell area markers (purple colors), Mmp2 (white) and Igf/Igfbp genes (blue colors), show increased extracellular matrix remodeling and IGF pathway activities around NMJ after denervation.

Fig. S7. Neuromuscular Junction Responses to Denervation.

(A-C) Expression of indicated genes across different experimental conditions, visualized by ViolinPlot (A, C) and DotPlot (B).

(D) Differential expression of postsynaptic nuclei markers across different clusters, visualized in DotPlot analysis.

(E-H) Identification of myofibers exhibiting day 3 denervated myofiber type I responses in muscle tissue at 7 day after denervation. Myofiber transcriptome identified by H&E-based segmentation was projected into histological space (E, left) and merged onto H&E image (E, right). D3-MF1 transcriptome, mostly present in day 3 denervated muscle (light blue) was found in day 7 denervated muscle tissue. Boxed area in (E) was magnified in (F-H). Indicated genes were plotted into the magnified space (F, G), and H&E histology show that area showing D3-MF1 transcriptome (yellow arrows) exhibits pale eosin staining, while areas showing D7-MF1 transcriptome (blue arrows) exhibit normal myofiber staining (H), suggesting subcellularly heterogenous degenerative responses localized around the NMJ area.

Fig 1. Hsu et al.

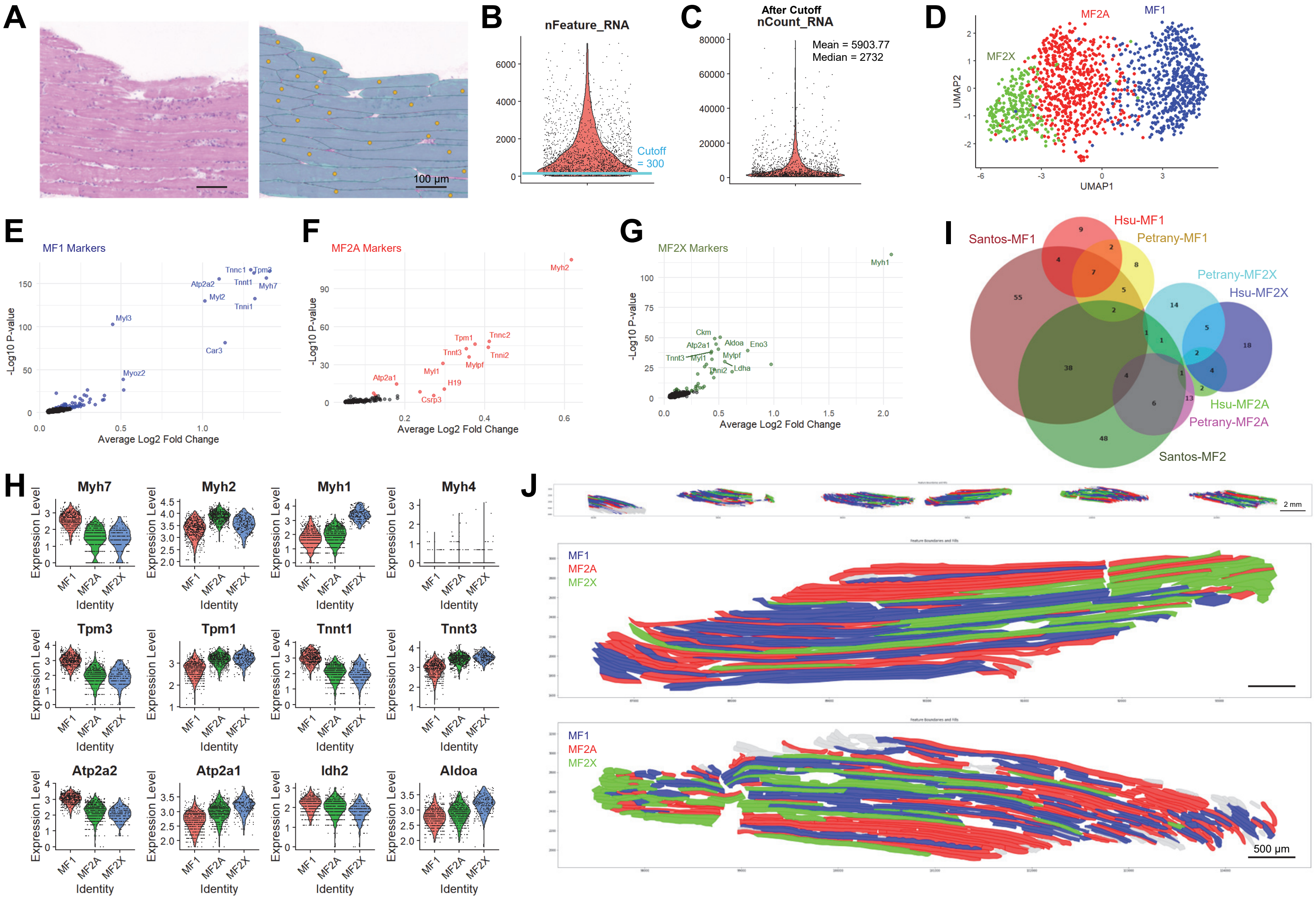

Fig S1. Hsu et al.

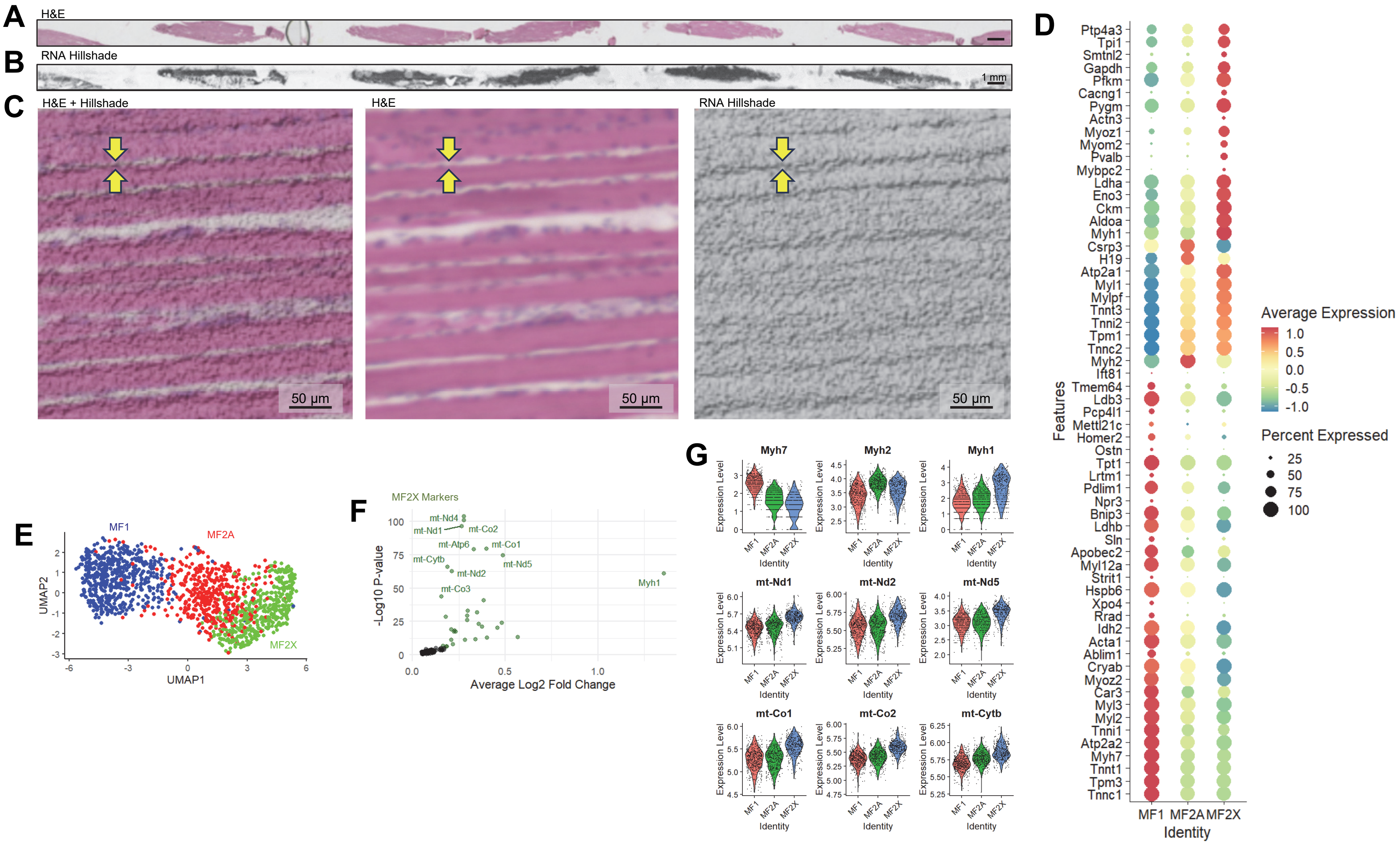

Fig 2. Hsu et al.

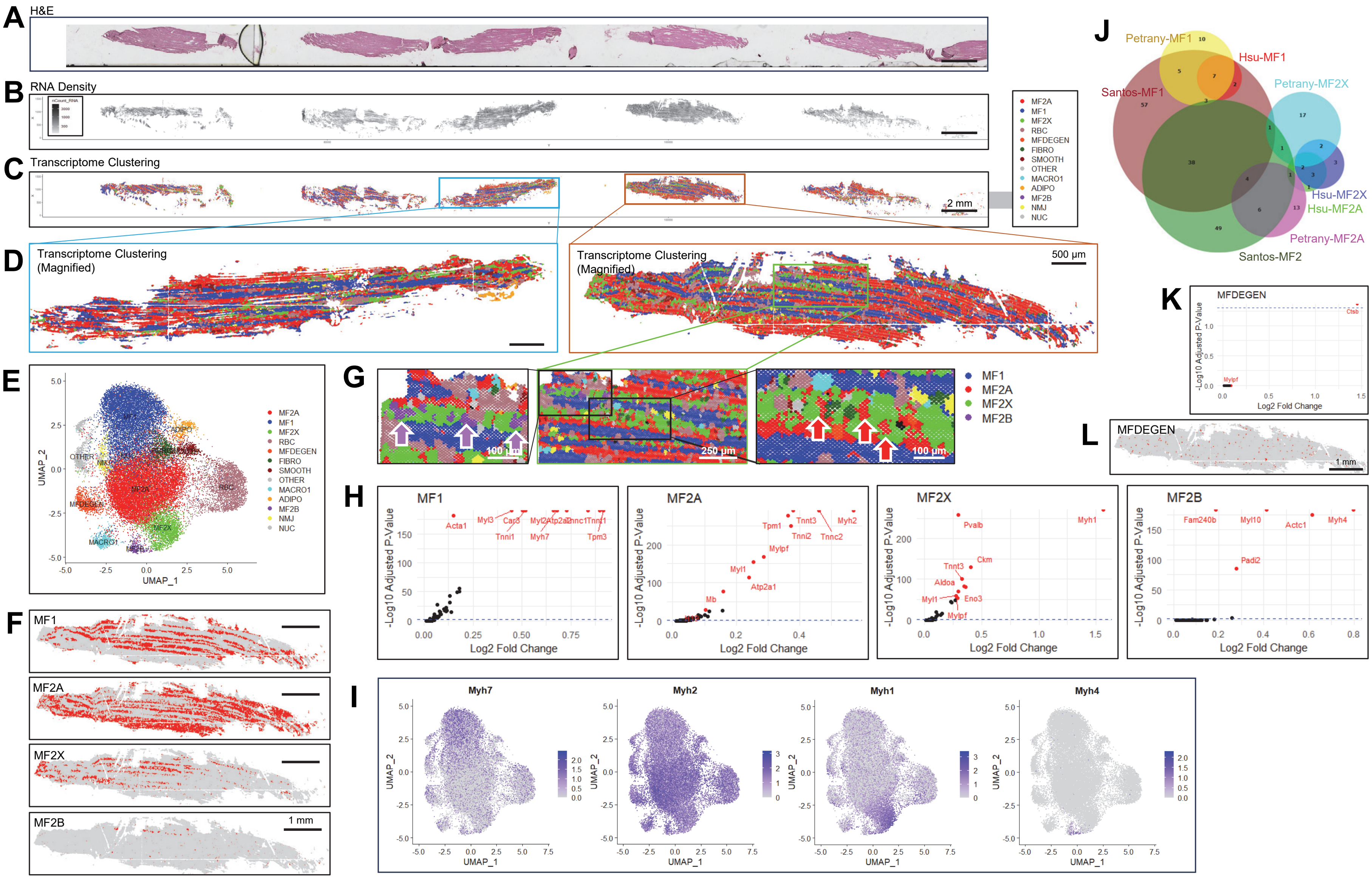

Fig S2. Hsu et al

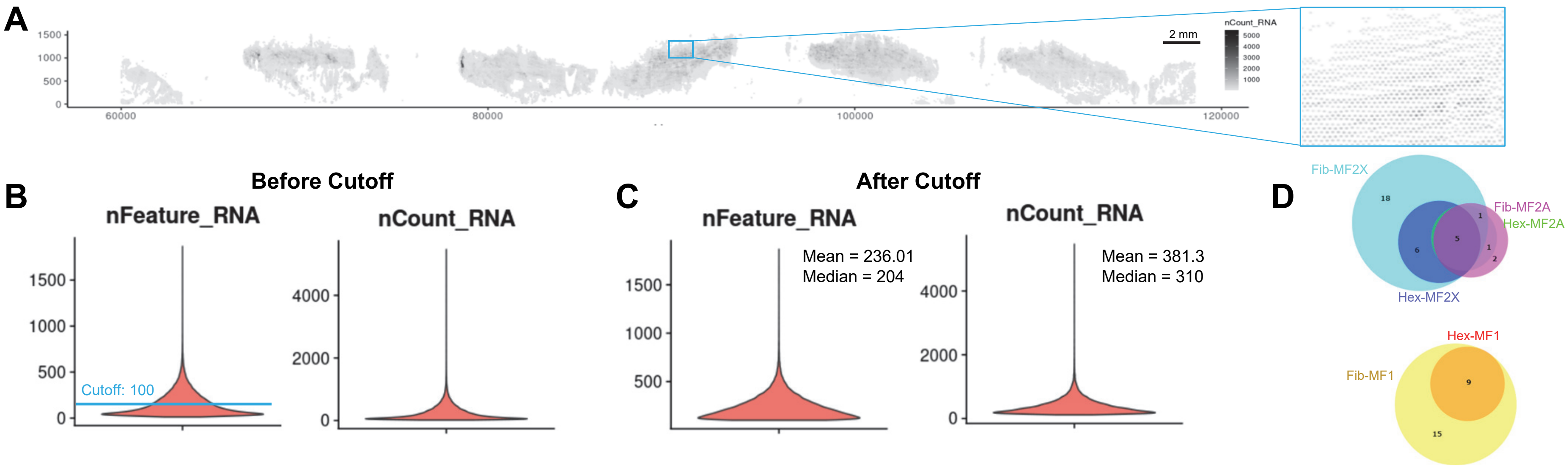

Fig 3. Hsu et al

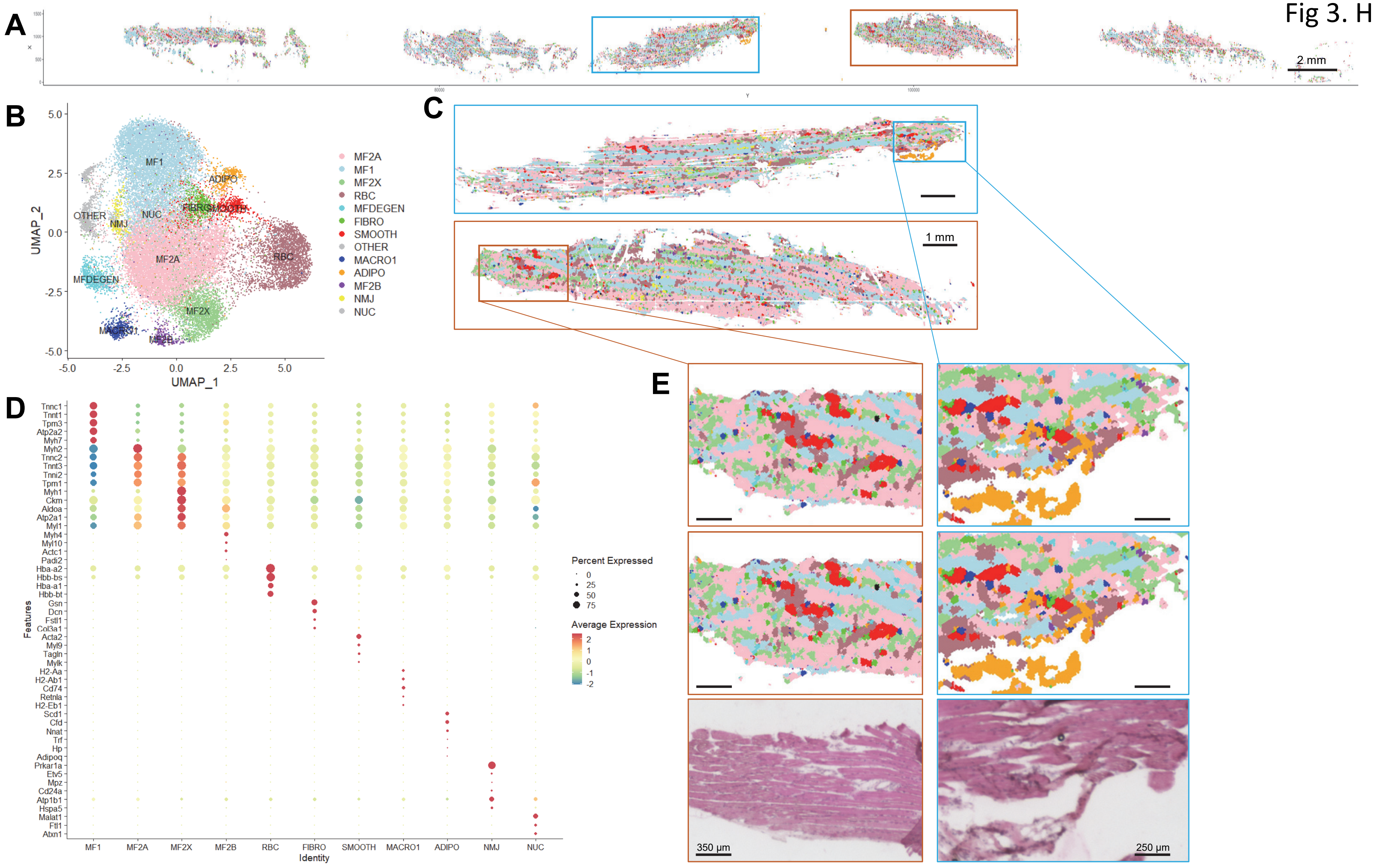

Fig S3. Hsu et al.

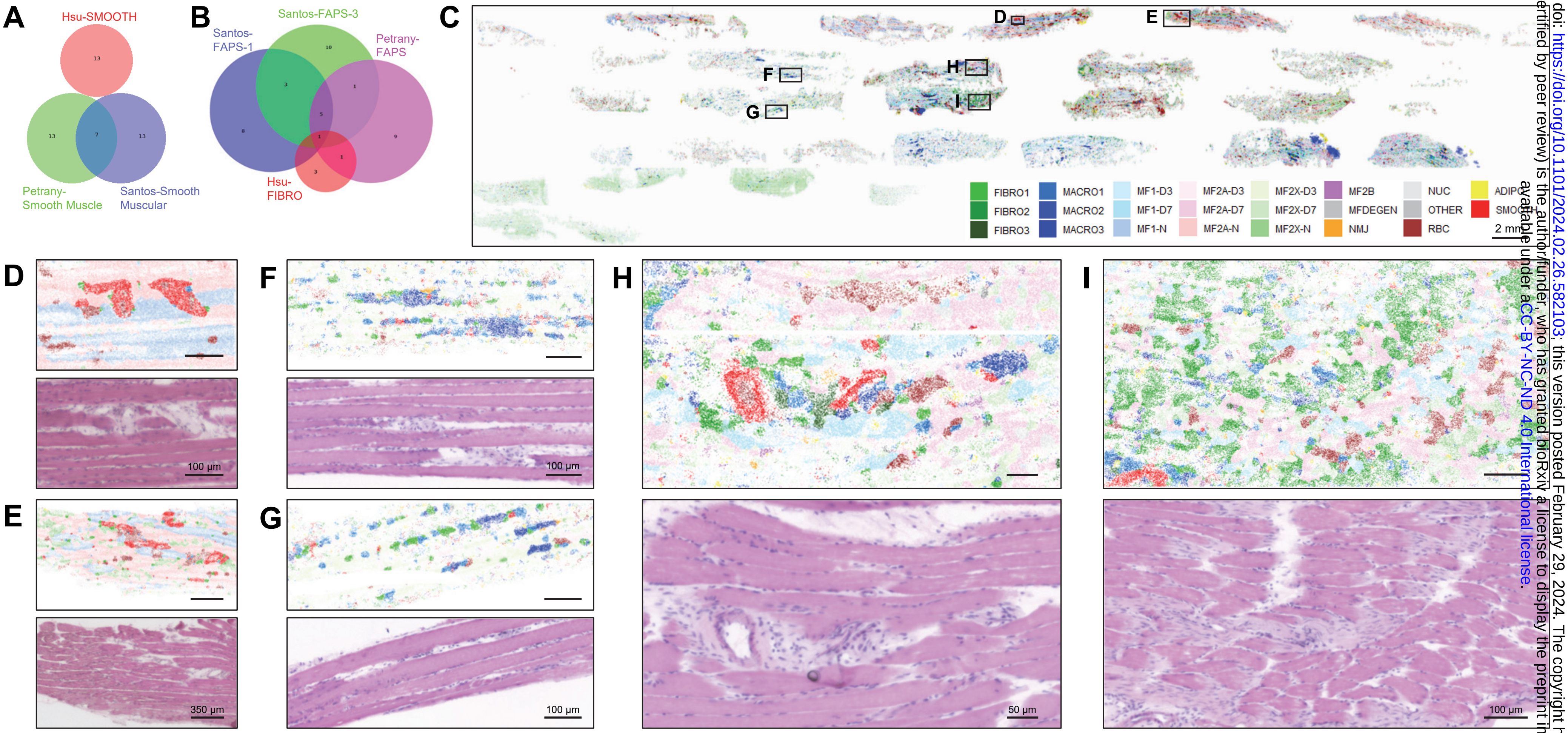

Fig 4. Hsu et al.

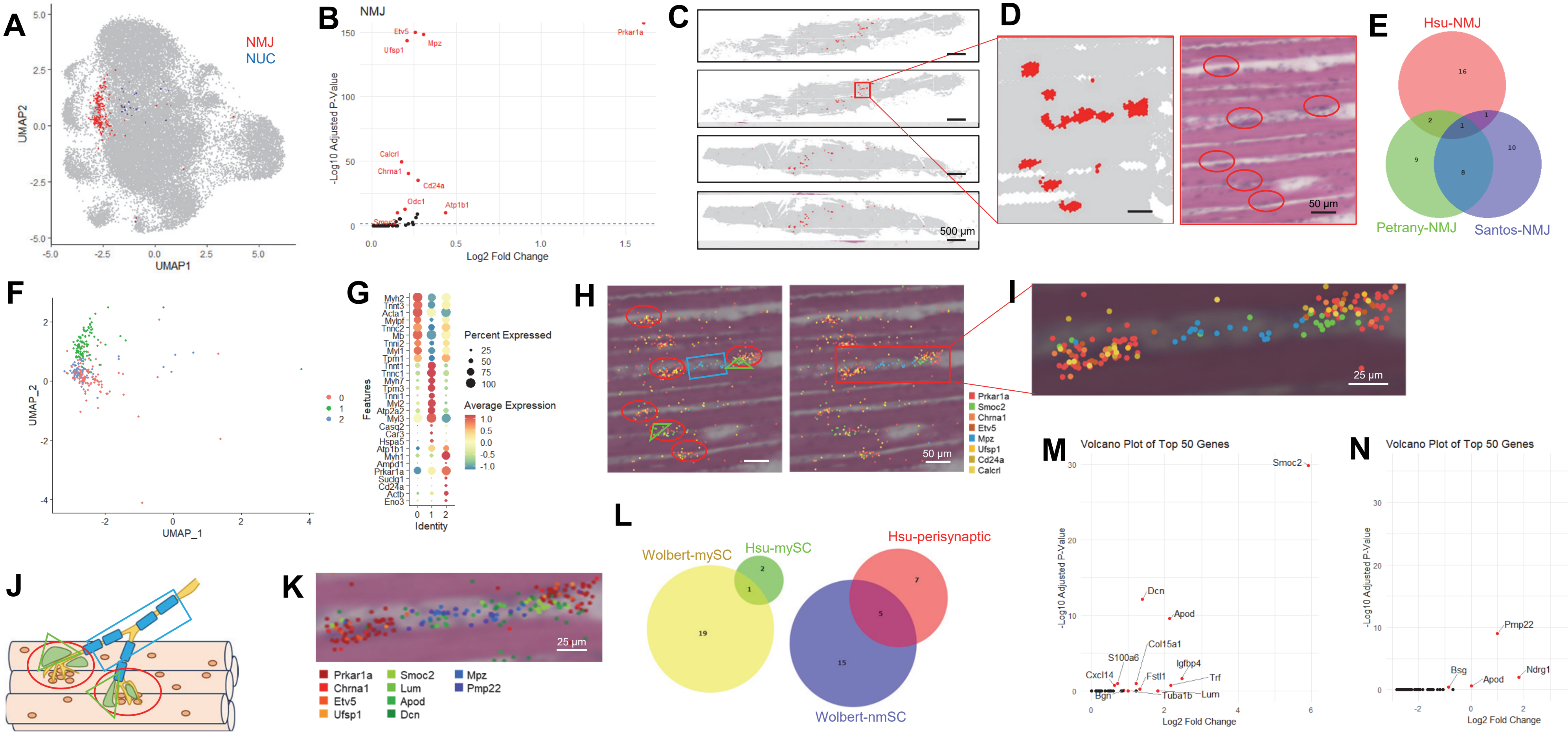

Fig S4. Hsu et al.

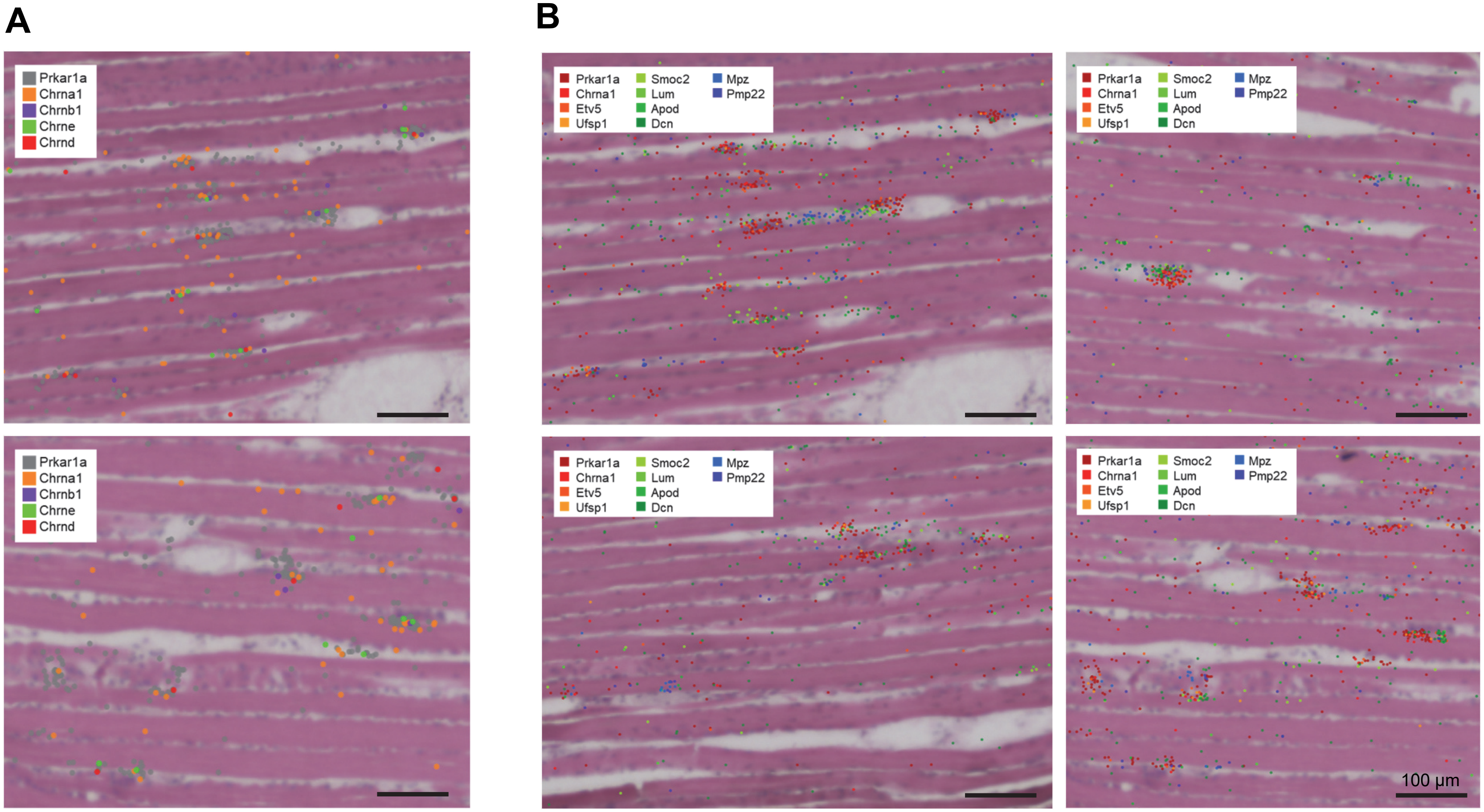

Fig 5. Hsu et al.

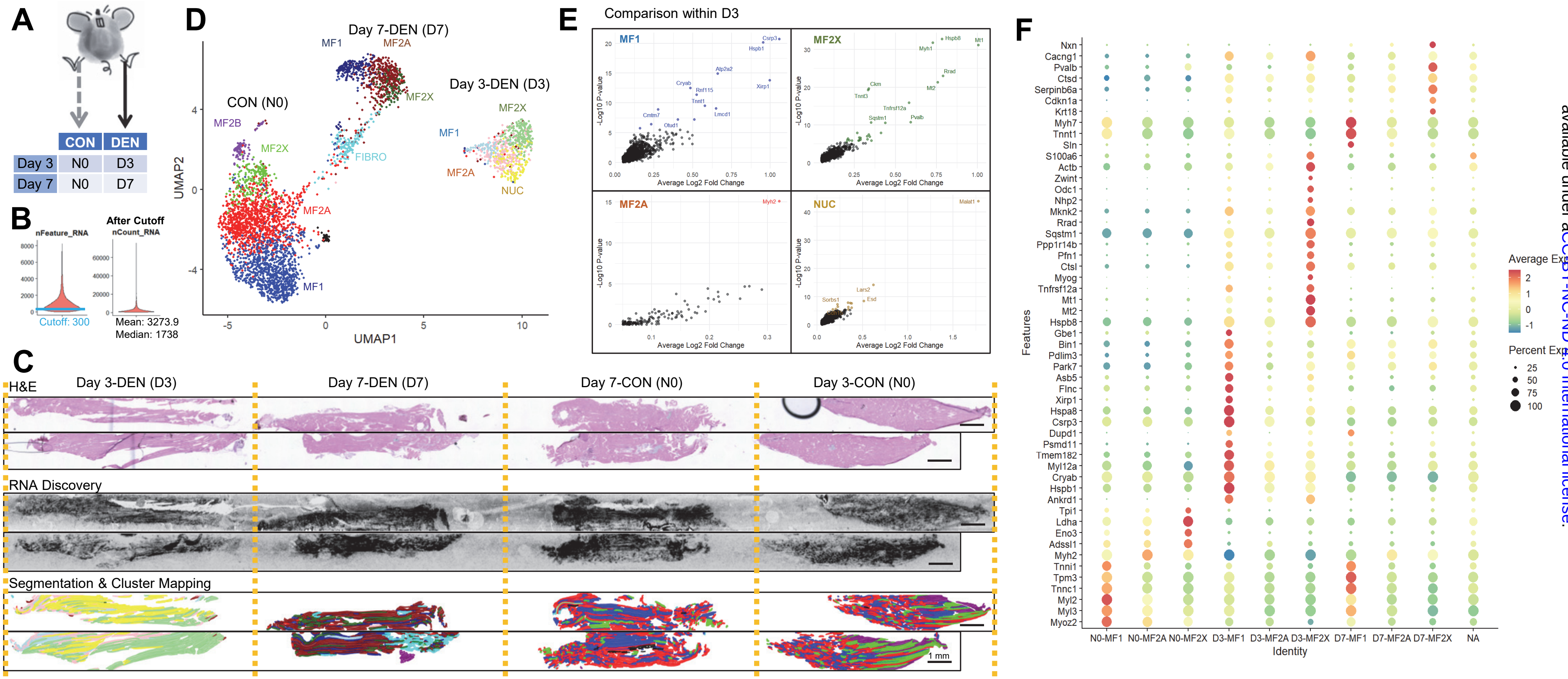

Fig S5. Hsu et al.

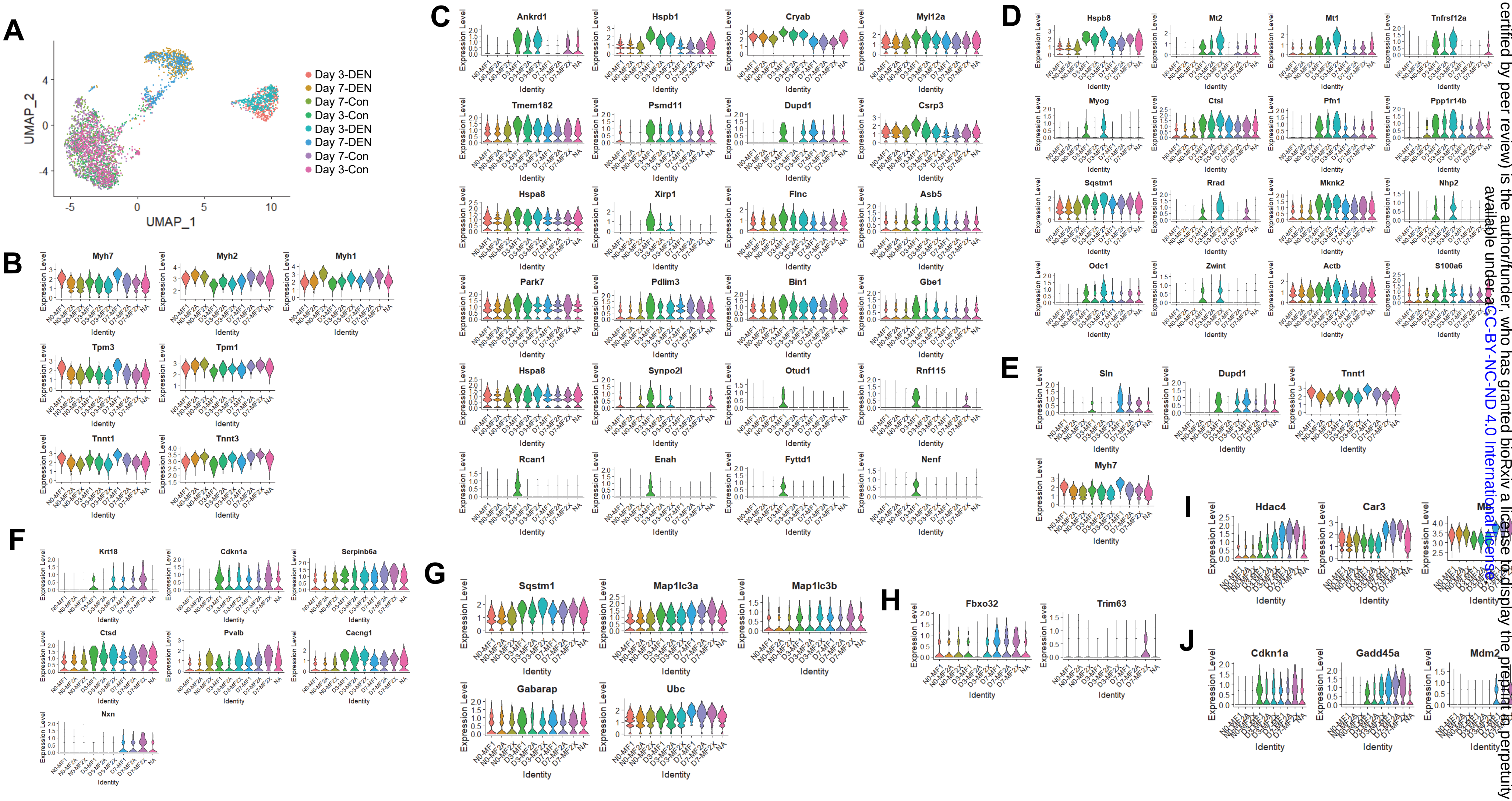

Fig 6. Hsu et al

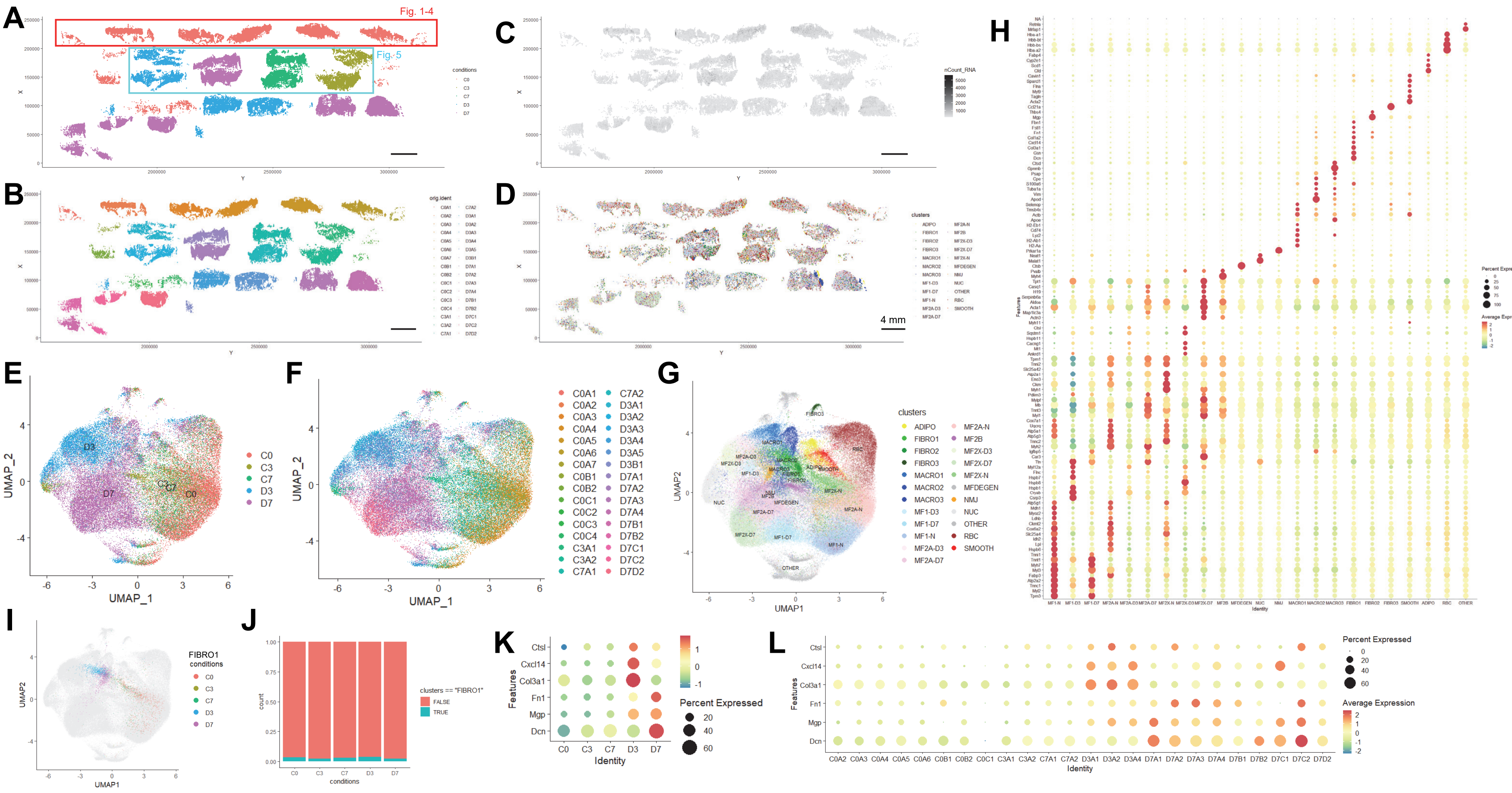

Fig S6. Hsu et al

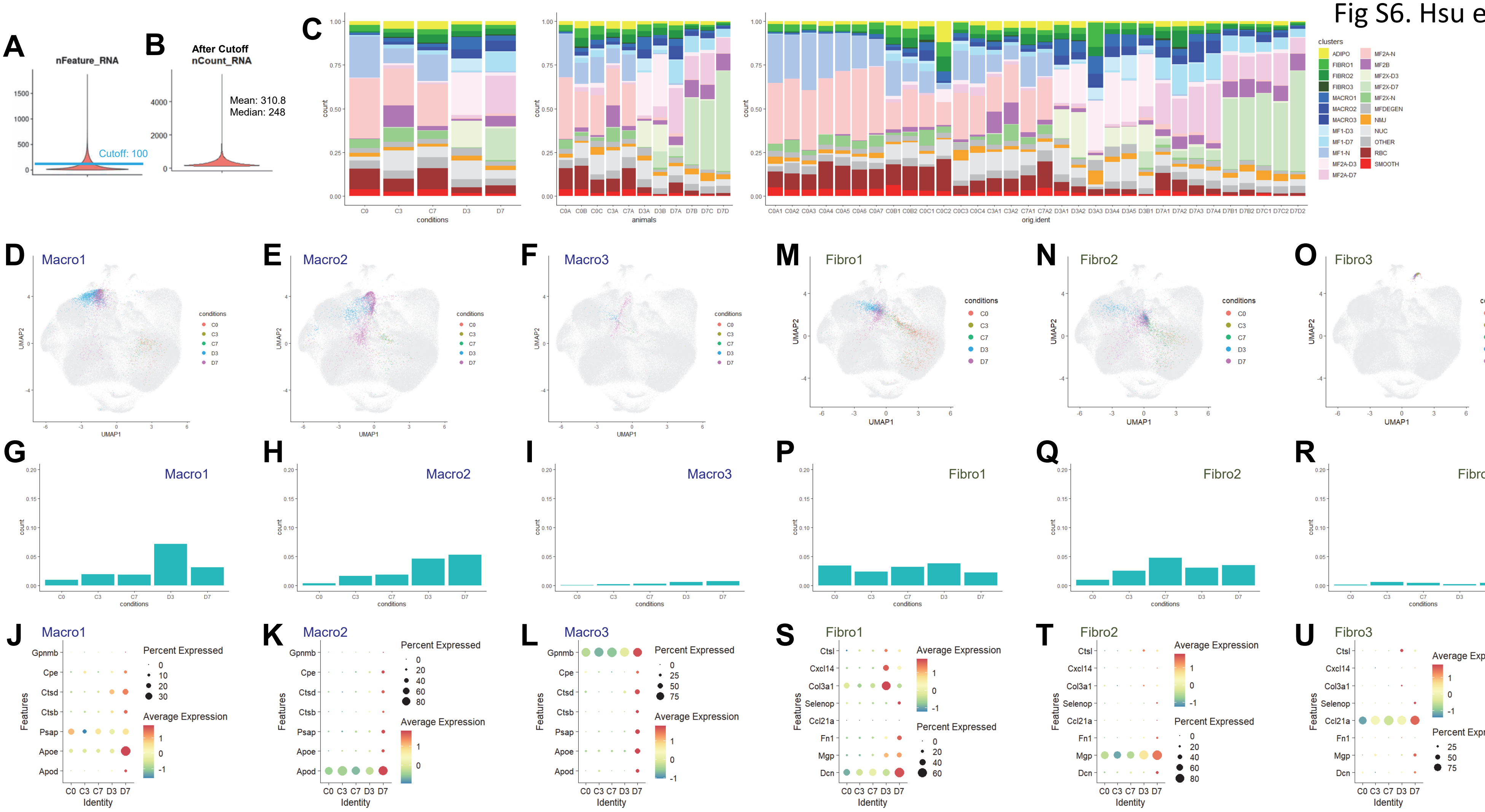

Fig 7. Hsu et al.

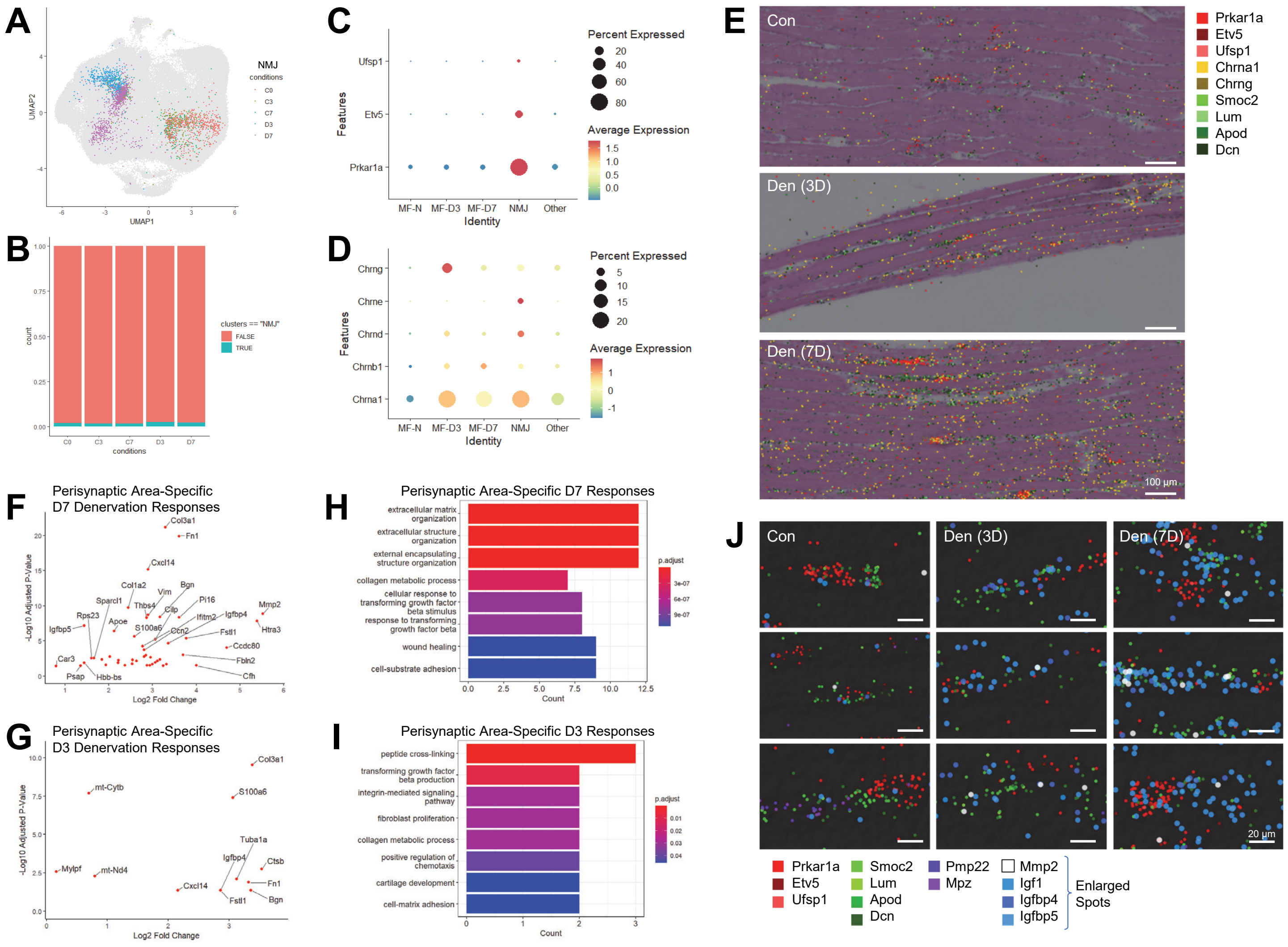

Fig S7. Hsu et al.